Monthly Notices
of the
ROYAL ASTRONOMICAL SOCIETY

MNRAS **487,** 2853–2873 (2019)
Advance Access publication 2019 May 31

doi:10.1093/mnras/stz1485

Synthetic molecular line observations of the first hydrostatic core from chemical calculations

Alison K. Young ,★ Matthew R. Bate , Tim J. Harries and David M. Acreman

Department of Physics and Astronomy, University of Exeter, Stocker Road, Exeter EX4 4QL, UK

Accepted 2019 May 23. Received 2019 May 23; in original form 2019 March 7

ABSTRACT

The first stable object to develop in the low-mass star formation process has long been predicted to be the first hydrostatic core (FHSC). Despite much effort, it has still yet to be definitively observed in nature. More specific observational signatures are required to enable observers to distinguish the FHSC from young, faint, but more evolved protostars. Here, we present synthetic spectral line observations for CO, SO, CS, and HCO^+ that were calculated from radiation (magneto)hydrodynamical models, chemical modelling, and Monte Carlo radiative transfer. HCO^+ $(1-0)$ and SO (8_7-7_6) spectra of the FHSC show variations for observations at a low inclination which may allow a candidate FHSC to be distinguished from a more evolved object. We find that the FHSC outflow is unlikely to be detectable with ALMA (Atacama Large Millimeter/Submillimeter Array), which would discount the observed sources with slow outflows that are currently identified as candidate FHSCs. We compare the results of simulated ALMA observations with observed candidate FHSCs and recommend Oph A SM1N and N6-mm as the most promising candidates to follow up.

Key words: astrochemistry – hydrodynamics – radiative transfer – stars: formation.

1 INTRODUCTION

The first hydrostatic core (FHSC) is the first stable object predicted to form during the gravitational collapse of a pre-stellar core (Larson 1969). The FHSC has a typical radius of ≈5 au but larger radii are possible with rotation (e.g. Bate 1998; Saigo & Tomisaka 2006; Bate 2011; Tomida, Okuzumi & Machida 2015). Magnetohydrodynamic (MHD) models have shown that the FHSC can launch a slow outflow (e.g. Tomisaka 2002; Banerjee & Pudritz 2006; Machida, Inutsuka & Matsumoto 2008; Bate, Tricco & Price 2014; Lewis & Bate 2017; Wurster, Bate & Price 2018) and that a magnetically supported pseudo-disc can form (e.g. Hennebelle & Fromang 2008; Commerçon et al. 2012). The FHSC lasts for a few hundred to a few thousand years, increasing in central density from $\sim 10^{-12}$ to $\sim 10^{-8}$ g cm^{-3}. When the central temperature reaches ∼2000 K, the molecular hydrogen dissociates and the second collapse begins. The central temperature and density increase rapidly and the second hydrostatic core, or stellar core, forms with a density of $\sim 10^{-2}$ g cm^{-3}.

This key stage of star formation is still yet to be observed definitively. The observational search for the FHSC has, however, produced several 'candidate FHSCs', for example B1-bN/bS (Pezzuto et al. 2012; Hirano & Liu 2014; Gerin et al. 2015; Fuente et al. 2017), CB17-MMS (Chen et al. 2012), and Aqu-MM1 (Maury et al. 2011; Young et al. 2018). A low-luminosity source ($\lesssim 0.1$ L$_\odot$) is usually identified as a candidate FHSC if it is faint or undetected at wavelengths $\lambda < 70$ μm and no outflow faster than 10 km s^{-1} is observed.

In recent years, attempts have been made to solve the problem of how to distinguish an FHSC from very faint, young protostars by simulating observations. Tomisaka & Tomida (2011) simulated CS line emission before and after FHSC formation using a fixed CS abundance and found the blue asymmetry characteristic of infall, signatures of a rotating outflow and that the linewidth increases after FHSC formation. Commerçon et al. (2012) examined the evolution of the spectral energy distribution (SED) of the FHSC and were not able to distinguish the FHSC from the newly formed stellar core. Commerçon et al. (2012) subsequently calculated synthetic Atacama Large Millimeter/Submillimeter Array (ALMA) dust emission maps which showed that ALMA would be able to resolve a fragmentating FHSC but could not reveal any difference between an FHSC and a stellar core. Young et al. (2018) produced synthetic SEDs for FHSCS with a range of physical properties and evolutionary stages and showed that SEDs are useful for selecting sources most likely to be FHSCs and placing constraints on their rotation rate, for example. Like Commerçon et al. (2012), they did not find any features to distinguish between SEDs of FHSCs and the stellar core. The above results indicate that high-resolution observations of molecular line emission are needed to identify the FHSC.

The physical conditions within the FHSC are very different to those of the collapsing core and so different chemical species are

★ E-mail: ayoung@astro.ex.ac.uk

expected to form in the FHSC. Furuya et al. (2012) modelled chemical evolution from a molecular cloud core to the FHSC and found that large organic molecules could be good tracers of the FHSC. Hincelin et al. (2016) also calculated chemical abundances as a post-process to a MHD model of a core collapse up to FHSC formation and examined the differences in chemical abundances between the different components, such as the core and disc. This work illustrates that different species may indeed trace different structures. The next step is to use calculated chemical abundances to simulate observations which could provide detailed diagnostics of the age of FHSCs and of the kinematic structures associated with them.

In this paper, we calculate chemical abundances by post-processing high-resolution smoothed particle hydrodynamics (SPH) simulations of the collapse of a pre-stellar core up to the formation of the stellar core. We then use these chemical abundances to simulate observations of selected molecular species.

2 METHOD

2.1 Hydrodynamical modelling

We model the collapse of a dense core until just after the formation of the stellar core using the SPH code SPHNG which originated from the code of Benz (1990) and was subsequently developed as described in Bate, Bonnell & Price (1995), Whitehouse, Bate & Monaghan (2005), Whitehouse & Bate (2006), and Price & Bate (2007). The models employ the radiative transfer method presented in Bate & Keto (2015) which combines the flux-limited diffusion method with additional interstellar medium (ISM) physics. This treats gas and dust temperatures separately and includes heating by the interstellar radiation field (ISRF) and cooling via line emission. Ideal MHD is included using the formalism of Price & Monaghan (2005), divergence cleaning (Tricco & Price 2012), and artificial resistivity (Tricco & Price 2013).

Two key types of structure associated with the FHSC are non-axisymmetric disc structures (e.g. spiral arms) and outflows. Magnetic fields are required to drive outflows (e.g. Bate et al. 2014; Lewis, Bate & Price 2015) but the magnetic braking effect of ideal MHD suppresses the formation of rotational structures (e.g. Bate et al. 2014). For this reason, we performed two simulations: first a radiation hydrodynamical (RHD) model, which we will refer to as the RHD model, to examine rotational structures and secondly a radiation MHD model, which we will refer to as the MHD model, to simulate observations of the outflow.

Both simulations start with a dense core that is modelled as a 1 $M_\odot$ Bonnor–Ebert sphere of radius 7×10^{16} cm ($\sim$4700 au), central density 8.34×10^{-18} g cm^{-3} using 3.5×10^6 SPH particles. The density contrast between the central and outer regions of the core was 15.1.

For the RHD model, an initial uniform rotation of $\Omega = 2.02 \times 10^{-13}$ rad s^{-1} was used, which gives a rotational to gravitational energy ratio $\beta = 0.02$, to produce an FHSC with non-axisymmetric features.

For the MHD model, we place the Bonnor–Ebert sphere in a warm, low density, cubic ambient medium of side length 2.8×10^{17} cm. The ratio of the density of the outer regions of the core and the ambient medium (the box) was 30:1, similar to the models of Bate et al. (2014). The initial mass-to-flux ratio is $\mu = 5$, $\Omega = 3.44 \times 10^{-13}$ rad s^{-1}, and $\beta = 0.05$. An outflow is launched from the FHSC and this extends to $\sim$150 au by the time the stellar core forms.

2.2 Chemical modelling

Chemistry calculations were performed using KROME (Grassi et al. 2014), which is a publicly available code for solving the kinetic equations of non-equilibrium gas-phase chemistry and is based on the DLSODES solver (Hindmarsh 1983). Adsorption and desorption reactions are included by considering the frozen-out species as separate species with their own abundances.

We calculate the chemical abundances by post-processing the SPH simulations. The total mass density, gas temperature, dust temperature, and extinction for each particle are provided by the SPH calculation for each time-step. KROME is called for each SPH particle and the chemistry is evolved for a time equal to the difference between the current and previous hydrodynamical outputs.

2.2.1 *Chemical network*

We combine the gas-phase KIDA[1] 2011 network (Wakelam et al. 2012), including grain charge transfer reactions, with gas-grain reactions from the network of Reboussin et al. (2014) which was based on that of Garrod, Wakelam & Herbst (2007). This includes both thermal desorption reactions and desorption induced by cosmic rays. The KIDA 2011 network was chosen over the 2014 network because it better matches the observed abundances of a greater number of species that we wished to model (with the exception of SO) (Wakelam et al. 2015). This gives a gas-grain network of 7009 reactions and 651 chemical species, where species frozen out onto the grain surface are counted separately. We neglect grain surface reactions, and therefore also desorption via exothermic surface reactions, to simplify the calculations and because they are much less significant for the simpler molecules considered here. The exception is the formation of H_2, for which we use the parameterization of the KIDA 2011 network.

The network contains reactions for temperatures up to 800 K but Wakelam et al. (2012) acknowledge that the gas-phase network has only been tested up to 300 K. This network is appropriate for the FHSC stage because gas temperatures only exceed 300 K within the FHSC itself. At stellar core formation, the gas temperature only exceeds 300 K within $\sim$3 au of the centre and exceeds 800 K within $\sim$ 1 au. These scales are unobservable due to the high densities. Emission from the very centre is mostly reprocessed by the surrounding material. Chemical abundances did not converge at the highest temperatures and densities within the FHSC so the last converged values are retained along with the time for which they were calculated. This is explained further in Section 2.2.2.

2.2.2 *Chemical evolution*

First we calculate the chemical evolution for dense, cold ISM conditions: $T = 10$ K, $\rho = 4 \times 10^{-18}$ g cm^{-3} ($n_{H2} \approx 10^6$ cm^{-3}), $A_v = 20$, cosmic ray ionization rate $\zeta = 1.3 \times 10^{-17}$ s^{-1}, and the elemental abundances given in Table 1 which were taken from Reboussin et al. (2014) and Hincelin et al. (2016). The dust grain abundance is calculated assuming a dust-to-gas ratio of 0.01 and that all dust grains have a negative charge initially. The initial electron abundance is found from the difference between the number density of cations and that of negatively charged grains such that the gas and dust have no net charge.

[1]KInetic Database for Astrochemistry.

Table 1. Elemental abundances used for the calculation of initial ISM abundances. These were mostly taken from Reboussin et al. (2014) and references therein and are very similar to the initial abundances of Hincelin et al. (2016) except for S^+. We use the higher S^+ abundance from the latter work.

Element	Abundance (n_j/n_H)
H_2	0.5
He	9×10^{-2} [a]
N	6.2×10^{-5} [b]
O	1.4×10^{-4} [c]
C^+	1.7×10^{-4} [b]
S^+	8×10^{-8} [d]
Si^+	8×10^{-9} [d]
Fe^+	3×10^{-9} [d]
Na^+	2×10^{-9} [d]
Mg^+	7×10^{-9} [d]
P^+	2×10^{-10} [d]
Cl^+	1×10^{-9} [d]

Notes. [a]Wakelam & Herbst (2008), [b]Jenkins (2009), [c]Hincelin et al. (2011), and [d]Graedel, Langer & Frerking (1982).

The chemical abundances calculated under the above conditions most closely matched those observed in the dense cores TMC-1 and L134N (Agúndez & Wakelam 2013) at $t = 1.2 \times 10^5$ yr. These abundances are therefore taken as the initial values and assigned to every SPH particle in the simulated dense core. Next, the chemistry was evolved for each particle in the initial Bonnor–Ebert sphere under their individual density, temperature, and extinction values for 60 000 yr, which is approximately the free-fall time of the core, to calculate the initial chemical abundances throughout the simulated dense core.

From this point, the new values of ρ, T_{gas}, T_{dust}, and A_v are provided by the SPH model for the next time-step and the chemical abundances calculated for the time between the current and previous time-steps. For the first ∼30 000 yr, during the first collapse, the physical conditions change little so it is unnecessary to calculate chemical abundances after every hydrodynamical time-step. After each chemistry time-step, the next minimum chemistry time-step is set relative to the local free-fall time: $\delta t = \frac{1}{3} t_{ff}$, where $t_{ff} = \sqrt{3\pi/32G\rho}$. The chemistry time-steps therefore decrease as the maximum density increases. During the first collapse stage the chemistry time-step decreases from $\delta t \approx 8000$ yr to a few hundred years. During FHSC phase, the chemistry time-step is ∼20–80 yr.

We note that the very centre of the core is ∼7 K initially which means that the network was extrapolated below its minimum temperature of 10 K. In the central regions of the core, the visual extinction of the ISRF becomes very large so a cap of $A_v = 86$ is implemented. This leads to effectively zero rates for reactions driven by UV photons for these regions.

As mentioned in the previous section, the chemical solver failed to converge at high densities. If the chemistry fails to converge for a particle the chemistry time-step is halved. If the chemistry does converge with the smaller time-step, KROME is called a second time for the particle with the same half-time-step such that the chemistry is evolved for the same net time-step. If the chemistry does not converge with the smaller time-step, the previous abundances are retained and the number of times the particle has failed to converge is recorded. The chemical model fails to converge within the centre of the FHSC, where $\rho \gtrsim 10^{-10}$ g cm^{-3}. This value is exceeded mid-way through the FHSC phase and within 2–3 au of the centre, or within 8 au near mid-plane of the disc in the RHD model. If the chemistry for a given SPH particle has failed to converge five times, or if $\rho > 10^{-10}$ g cm^{-3}, the chemistry calculation is skipped and the current abundances are retained. All unconverged particles lie inside the FHSC and, for the RHD model, comprise only 1.7 per cent of the total mass during the FHSC stage and 2.8 per cent of the total mass after stellar core formation. These values are very similar for the MHD model. Since we are interested in modelling observational properties, the chemistry of the centre of the FHSC is inconsequential because the FHSC is extremely optically thick and submillimetre emission from this region would be reprocessed before reaching the observer.

2.3 Radiative transfer

We took snapshots from the chemical post-processing of the hydrodynamical models to synthesize the line emission of selected molecular species with TORUS. TORUS is a Monte Carlo radiative transfer code that has been frequently applied to dust continuum and line-transfer simulations of star formation and protostellar discs (e.g. Harries 2000, 2011). First the adaptive mesh refinement (AMR) grid is populated from the SPH particles following the method described by Rundle et al. (2010). The SPH particles were mapped onto the cubical AMR grid of side length 6×10^{15} cm (400 au) and mass resolution of 10^{27} g per grid cell for the radiative transfer modelling, with the exception of the HCO^+ models. The density and temperature are low enough outside this region that the contribution to the spectrum is negligible relative to the contribution from the inner few tens of au. There is, however, a significant contribution from the envelope to the $HCO^+(1-0)$ spectrum, therefore a larger grid of 8×10^{16} cm (5350 au) with a coarser mass resolution (10^{28} g per cell) was used for this transition.

The level populations were calculated assuming local thermodynamic equilibrium (LTE) and are calculated iteratively from the radiation incident on each cell. This is a valid assumption here because the density in the simulated collapsing cloud is higher than the critical density for the species and transitions considered. A Monte Carlo method is used to follow the emission and absorption of continuum and line photon packets through the model to an observer. A turbulent line broadening of 0.1 km s^{-1} is applied. A position–position–velocity (PPV) FITS image cube is produced for an observer at 150 pc. The PPV cubes have a side length of 370 au and 81 channels from −4 to 4 km s^{-1}, giving a channel width of 0.1 km s^{-1}.

The silicate dust grain type of Draine & Lee (1984) with a power-law distribution of grain sizes between 0.1 and 1 μm of $n(a) \propto a^{-q}$ with $q = 3.5$ (Mathis, Rumpl & Nordsieck 1977) was used to calculate the dust extinction, continuum emission for the continuum images, and the continuum contribution to the spectra.

2.4 Processing image files

The PPV cubes generated straight from TORUS are noise-free so it is sufficient to perform the continuum subtraction with just one line-free channel. Integrated intensity maps were constructed from the continuum-subtracted PPV cubes by summing the channels as follows, where Δv is the channel width:

$$I = \sum_{v=1}^{n} I_v \Delta v. \quad (1)$$

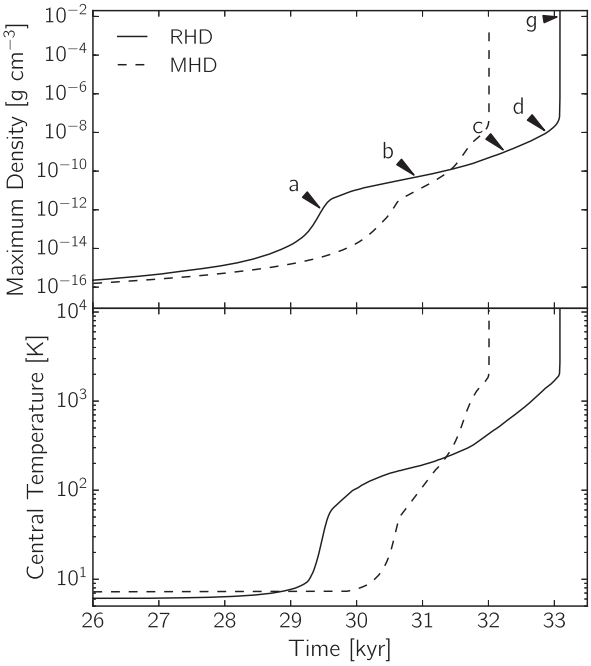

Figure 1. The time evolution of the maximum density (top) and central temperature (bottom) for the RHD model (solid lines) and MHD model (dashed lines). Snapshots were taken from these models at certain values of maximum density for comparing evolutionary stages and simulating observations. These are indicated for the RHD model. Snapshot (a) is taken just before the FHSC forms. The density and temperature increase more slowly after this point before rapidly increasing again during the second collapse.

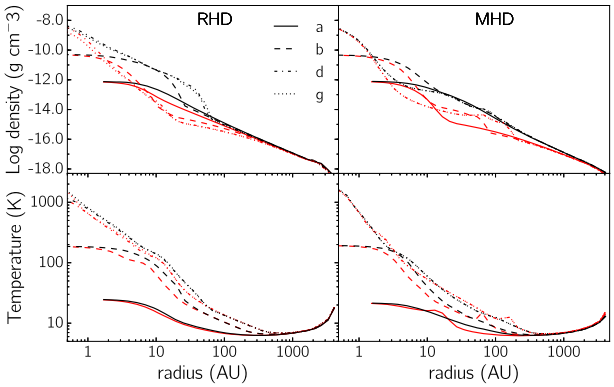

Figure 2. Density and temperature radial profiles for the RHD and MHD models at snapshots (a) before FHSC formation, (b) and (d) during the FHSC stage, and (g) after the formation of the stellar core. Profiles are shown parallel to the rotation axis (black) and perpendicular to the rotation axis (red).

Spectra were calculated by averaging pixels within a 0.35 arcsec diameter aperture for CS and SO, and within a 0.67 arcsec aperture for CO and HCO^+ for which the emission is more extended.

ALMA observations were simulated from the PPV cubes using the `simalma` routine in CASA (McMullin et al. 2007). Channels corresponding to -4.0 to $-3.5\,\mathrm{km\,s^{-1}}$ and 3.5 to $4.0\,\mathrm{km\,s^{-1}}$ for which there was no line emission were averaged and subtracted from all channels to remove the continuum emission.

Position–velocity (PV) diagrams were constructed for CO PPV cubes to examine rotation. The PV cuts were taken perpendicular to the rotation axis, through the mid-plane of the disc or pseudo-disc. The brightness of each velocity channel at each position was calculated by adding the intensity of pixels within $\pm$ 0.15 arcsec above and below this centre line.

3 RESULTS

3.1 Morphology and velocity structure of the hydrodynamical models

The evolution of the maximum density and central temperature are presented in Fig. 1. Initially, the temperature is lowest at the centre of the core and the temperature remains $\approx$15 K at the edge throughout the simulation due to heating by the ISRF. It is therefore more useful to compare the central temperature rather than maximum temperature. The FHSC forms after 29 500 yr in the RHD model and after 30 700 yr in the MHD model. The FHSC is deemed to have formed when the rapid increase in central density and temperature that occurs during first collapse ceases and the density and temperature continue increasing at a slower rate (just after point (a) in Fig. 1). The FHSC lasts for 3500 yr in the RHD model and for 1300 yr in the MHD model. The lifetime is shorter in the MHD model because magnetic braking slows the rotation such that the rotational support is reduced.

We take snapshots from the hydrodynamical models at selected times to allow comparison of the synthetic observations for different evolutionary stages. These are taken at the following values of the central density: (a) $10^{-12}\,\mathrm{g\,cm^{-3}}$, (b) $5 \times 10^{-11}\,\mathrm{g\,cm^{-3}}$, (c) $10^{-9}\,\mathrm{g\,cm^{-3}}$, (d) $10^{-8}\,\mathrm{g\,cm^{-3}}$, and (g) $10^{-2}\,\mathrm{g\,cm^{-3}}$ (these are the same values as used in Young et al. 2018). Snapshot (a) is taken just before FHSC formation, (b)–(d) are during the FHSC stage, and (g) is taken just after the formation of the stellar core. Density and temperature profiles for four key evolutionary stages are presented in Fig. 2. It is important to note that the temperature remains $<$100 K at $r > 10$ au even at snapshot (g), i.e. shortly after stellar core formation, and $T < 300$ K at $r > 4$ au (see Fig. 2) which means the chemical network is valid for observable size scales.

The morphology of the RHD and MHD models is shown in Fig. 3. In the RHD model (upper two panels), the FHSC has the form of a rotationally supported disc which increases in radius from $\sim$20 to $\sim$35 au (cf. Bate 1998, 2011). Late in the FHSC stage, after 32 000 yr, a spiral instability develops. The disc is also apparent in the diagrams of the velocity structure shown in Fig. 4 (upper panels), as well as the infall perpendicular to the plane of the disc. After second collapse and the formation of the second (stellar) core, the disc and spiral structures persist.

In the MHD model, the FHSC forms after 30 700 yr. The cloud core is initially rotating quickly in this model but the rotation is significantly reduced by magnetic braking and the FHSC is not rotationally supported. A pseudo-disc forms around the FHSC, comprised of gas with infalling, rotating motions (see Fig. 4). An outflow is launched around 400 yr after FHSC formation, the structure of which is shown in Fig. 3 (lower panels), and the lower panels of Fig. 4. Outflow velocities reach 0.5–1.0 $\mathrm{km\,s^{-1}}$ at distances of 20–150 au from the mid-plane. Infall continues through the pseudo-disc at $|v| \leq 0.5\,\mathrm{km\,s^{-1}}$ and also vertically within $r < 10$ au with velocities exceeding $1\,\mathrm{km\,s^{-1}}$. The line-of-sight rotational velocities in the outflow and pseudo-disc are similar to the outflow and infall velocities which means that all of these regions must be considered to understand the nature of the spectra.

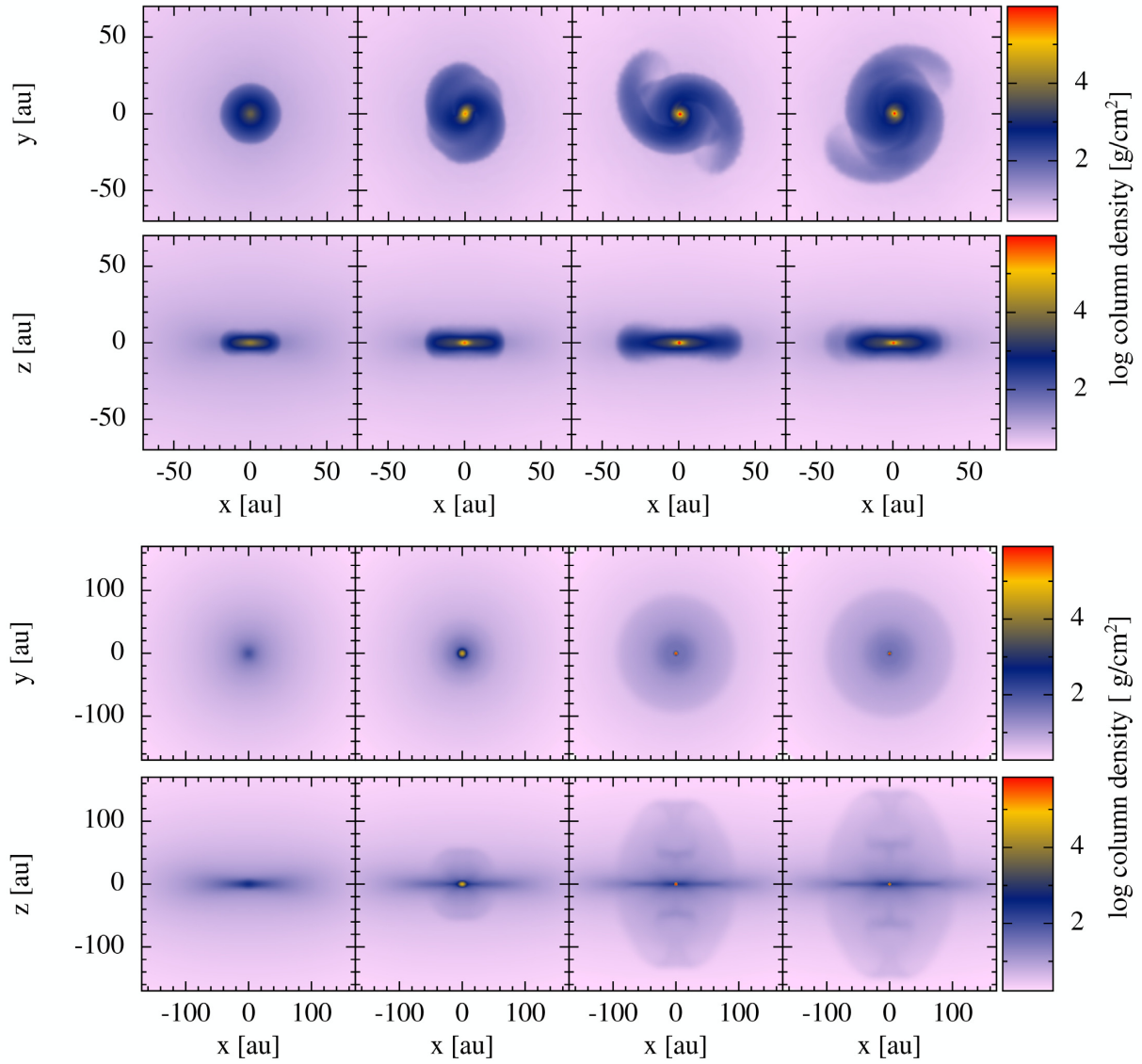

Figure 3. Evolution of the RHD model viewed at $i = 0°$ and 90° (upper two rows) and the MHD model also viewed at the same inclination angles (lower two rows). From left to right, (b)−(d) panels show FHSC snapshots and (g) the stellar (second) core snapshot. The development of spiral structure is apparent in the RHD model and the outflow is seen in the MHD model at $i = 90°$.

Infall velocities reach $\sim$3 km s^{-1} in the RHD model but are lower in the MHD model due to additional magnetic pressure and remain $<$1.5 km s^{-1} after stellar core formation.

3.2 Chemical evolution

Chemical abundances as a function of radius for the RHD case are shown in Figs 5 and 6. From here on we refer to chemical abundances relative to the abundance of molecular hydrogen. Other species with high abundances not shown here include CCH, HCN, HNC, and H_2O. Some interesting species such as methanol and formaldehyde form primarily through grain surface reactions and so we cannot calculate realistic abundances for these. The abundances beyond 100 au remain mostly unchanged throughout FHSC phase and stellar core formation because the temperature and density change very little. However, for nearly all the species shown, there is a dramatic change at $r \lesssim 30$ au when the FHSC forms and the gas-phase abundances increase quickly. We note that the abundances of the species discussed here are also high at large radii in the envelope and surrounding molecular cloud. However, if we select transitions that are excited at the higher temperatures of the warm core then it is only the abundances towards the centre of the cloud core that matter for observations.

The abundance of CS peaks sharply within a radius of a few au, indicating that it traces the warmest region at the centre of the FHSC. The peak abundance increases significantly during the FHSC stage so we may expect to see CS lines brighten as the core evolves. CN traces a similar region but its central abundance increases later than CS. The abundance of H_2CN increases rapidly within the FHSC and becomes 4–5 orders of magnitude higher than in the surrounding envelope, which may provide an indication of the FHSC.

OCS, SO, and CO trace the FHSC but to different radii. In the RHD model, these species trace regions within $\sim$ 15, 20, and 30 au, respectively, in the disc plane. For these species, the peak abundance

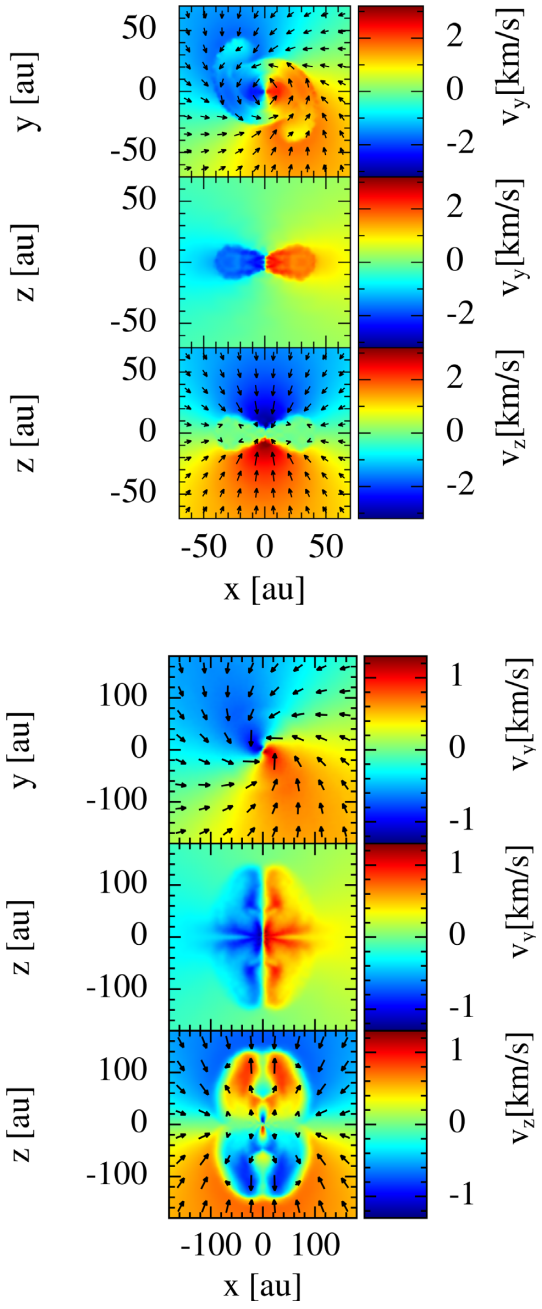

Figure 4. Velocity structure at snapshot (d) (late FHSC) Upper panels: RHD model. Cross-section of the velocity component approaching an observer viewing the system edge-on, v_y, in the mid-plane (top) showing a rotationally supported disc; v_y, as viewed edge-on (centre); and the vertical component of the velocity, v_z (bottom). Arrows show the direction of the net velocity. Lower panels: as above but for the MHD model. The key features are the rotating pseudo-disc and outflow. The highest velocities are due to infall within ±20 au.

does not change after the FHSC forms but the radius within which the abundance is high increases as the disc warms up. For example, CO desorbs from dust grains as soon as the FHSC forms and the size of the disc traced by CO increases from ∼15 to ∼30 au in the first half of the FHSC phase. OCS follows the same pattern but traces the disc to a smaller (<15 au) radius.

Abundances in the MHD model (Figs 7–9) are similar except in the vertical direction after the outflow is launched. HCO^+ and CO are abundant out to larger radii in the vertical direction than the horizontal due to the outflow. SO still appears to trace the central core well since the abundance decreases by several orders of magnitude at 10 au even in the direction of the outflow. In the MHD model, the peak abundance of SO increases by a factor of 10 during FHSC stage.

The abundance of HCO^+ is lowest in the centre of the core after FHSC formation and increases with radius. There is a region of enhanced HCO^+ abundance within a shell at ∼10–50 au. The abundance of HCO^+ is lower in the outflow than surrounding envelope and lower still in the pseudo-disc. HCO^+ is therefore likely to trace the inner envelope structure, but not the disc or pseudo-disc.

The abundance of NH_3 peaks within the FHSC in the MHD model and to a lesser extent also in the RHD model. NH_3 is depleted to a radius of ∼100 au within the pseudo-disc and within the outflow. In the RHD model, NH_3 is depleted within the spiral arms but the abundance is high within a radius of $r \lesssim 30$ au and is high in the envelope.

Abundances of the other species here peak sharply in the centre, except for SO which traces out to 8 au above the mid-plane and CO which traces out to 20 au. At this distance, CO should trace the base of the outflow but SO is more likely to trace the infall close to the centre of the core.

The chemical abundances within and close to the FHSC are very different to the abundances in the centre of the pre-stellar core before FHSC formation because many species desorp from the dust grains with the rapid increase in temperature. For both models, the species that show significant evolution in abundance during the FHSC stage are CS, NH_3, and SO. The abundance of OCS in the centre of the core decreases during FHSC stage in the MHD model.

For all species considered here, clues to the evolutionary stage of the core are likely to be given by changes in envelope structures revealed by certain species rather than by changes in chemical abundances alone. Murillo et al. (2018) conclude from observations of two Class 0 protostars that temperature is a key factor in driving the chemical composition of a protostellar envelope. Since the temperature structures are similar, it is likely that the kinematics rather than the chemical abundances will prove a better diagnostic of the FHSC.

3.3 Synthetic observations

In this section, we present synthetic observations of CO (4 − 3) (461.041 GHz), SO (8_7 − 7_6) (340.714 GHz), CS (8 − 7) (391.847 GHz), and HCO^+ (1 − 0) (89.198 GHz). These species are expected to have high enough abundances to be detectable and to trace different structures. CS also shows a significant change in abundance as the FHSC grows. CN, NH_3, and N_2H^+ are also likely to trace FHSC structures. However, at the moment we are unable to compute the hyperfine structure lines necessary to model the emission from these molecules.

3.3.1 Continuum

The 230 GHz continuum image of the late FHSC from the RHD model is presented in Fig. 11 to allow comparison with line observations. The continuum emission here is tracing the denser regions such that the centre of the FHSC appears bright and the spiral structures are only visible within 20 au.

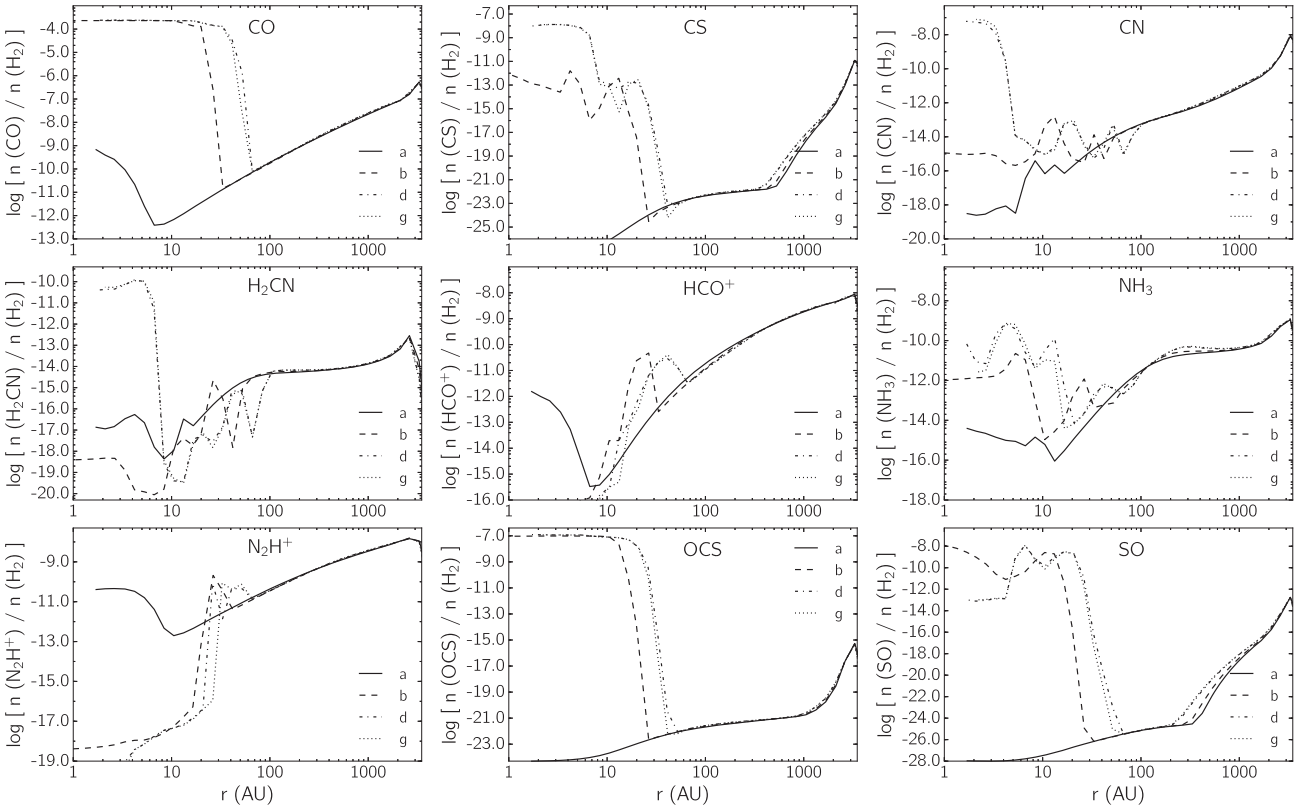

Figure 5. Average abundances of selected species calculated for the RHD model perpendicular to the rotation axis.

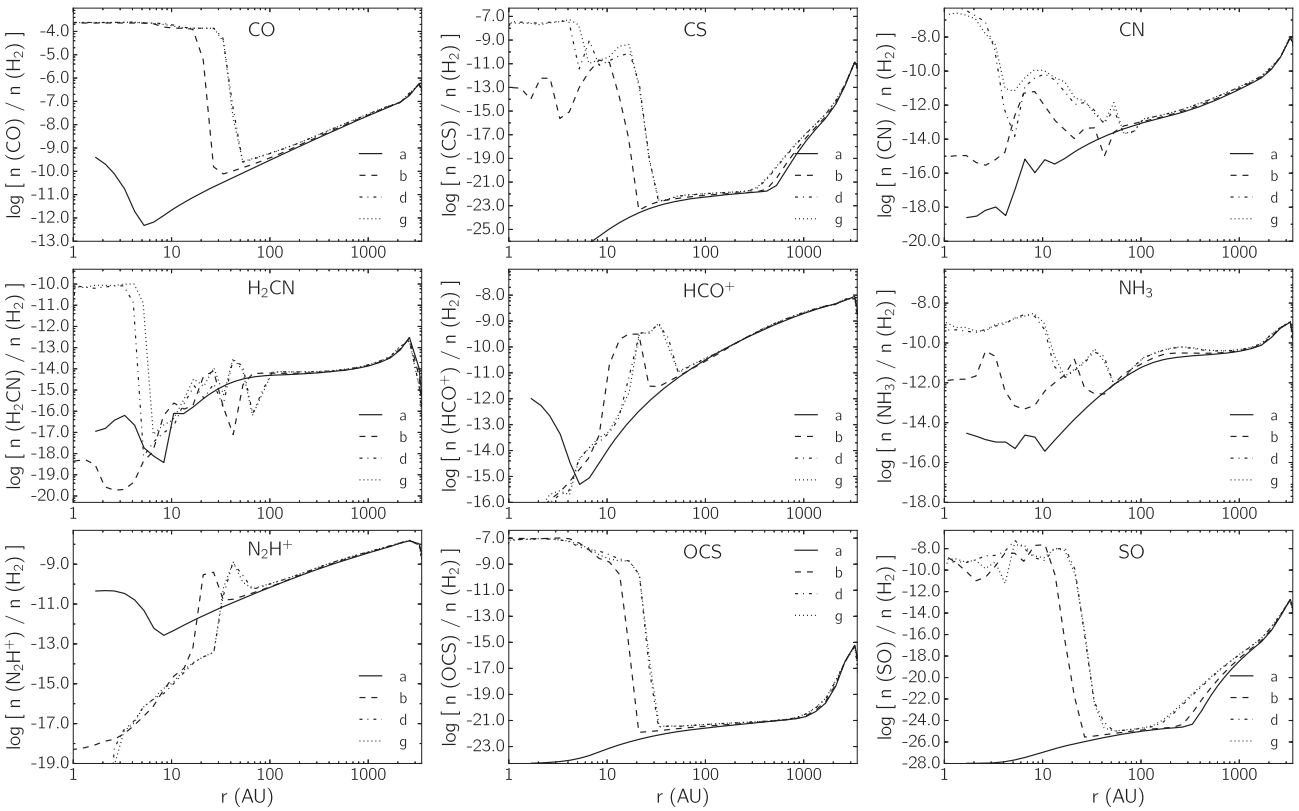

Figure 6. Same as for Fig. 5, but in the vertical direction (parallel to the rotation axis).

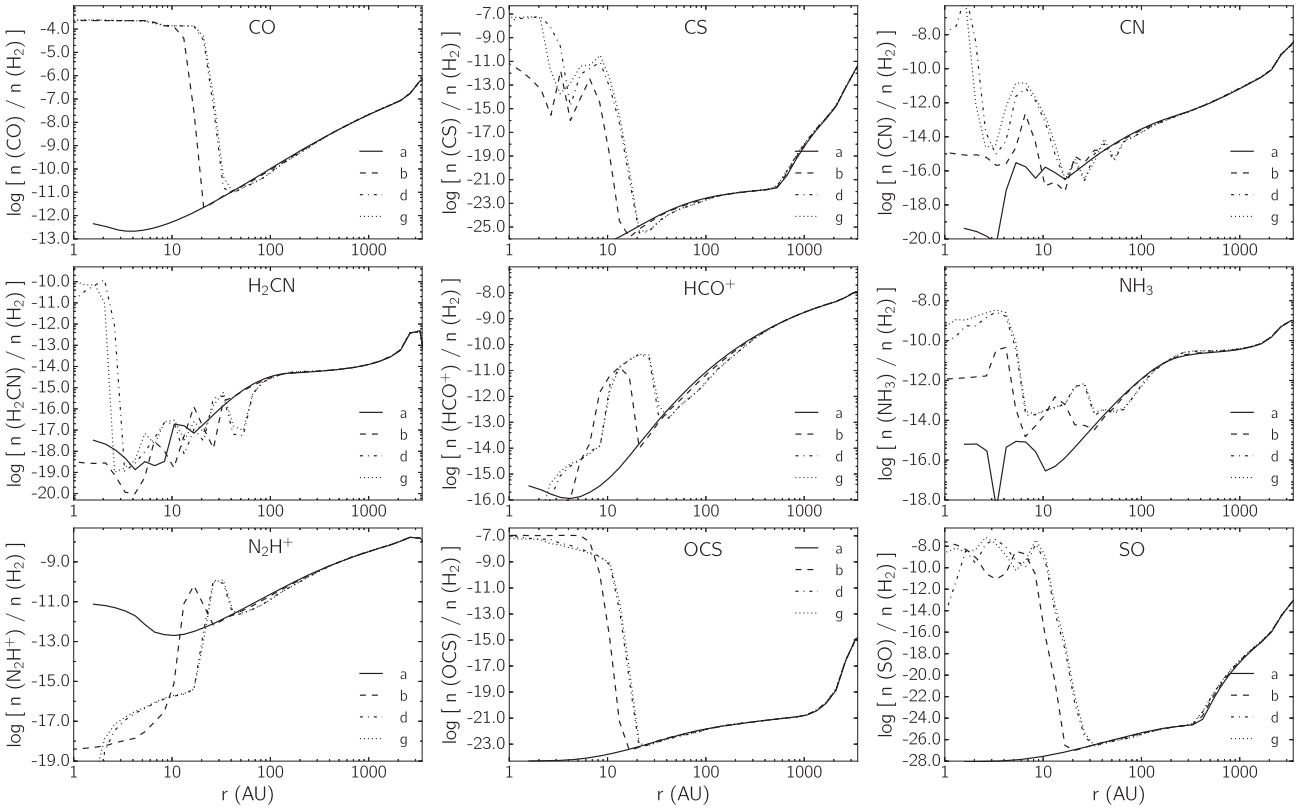

Figure 7. Average abundances of selected species from the MHD model perpendicular to the rotation axis.

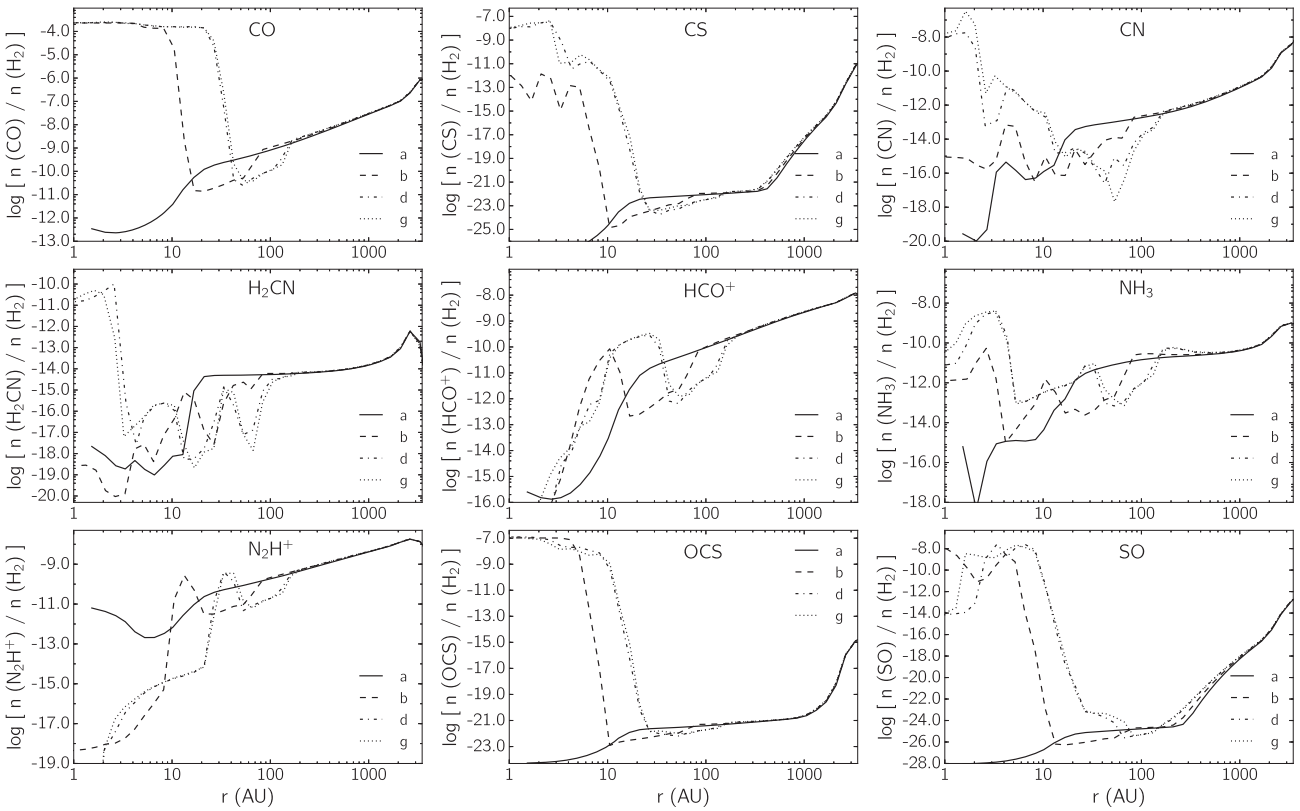

Figure 8. Same as for Fig. 7 in the vertical direction.

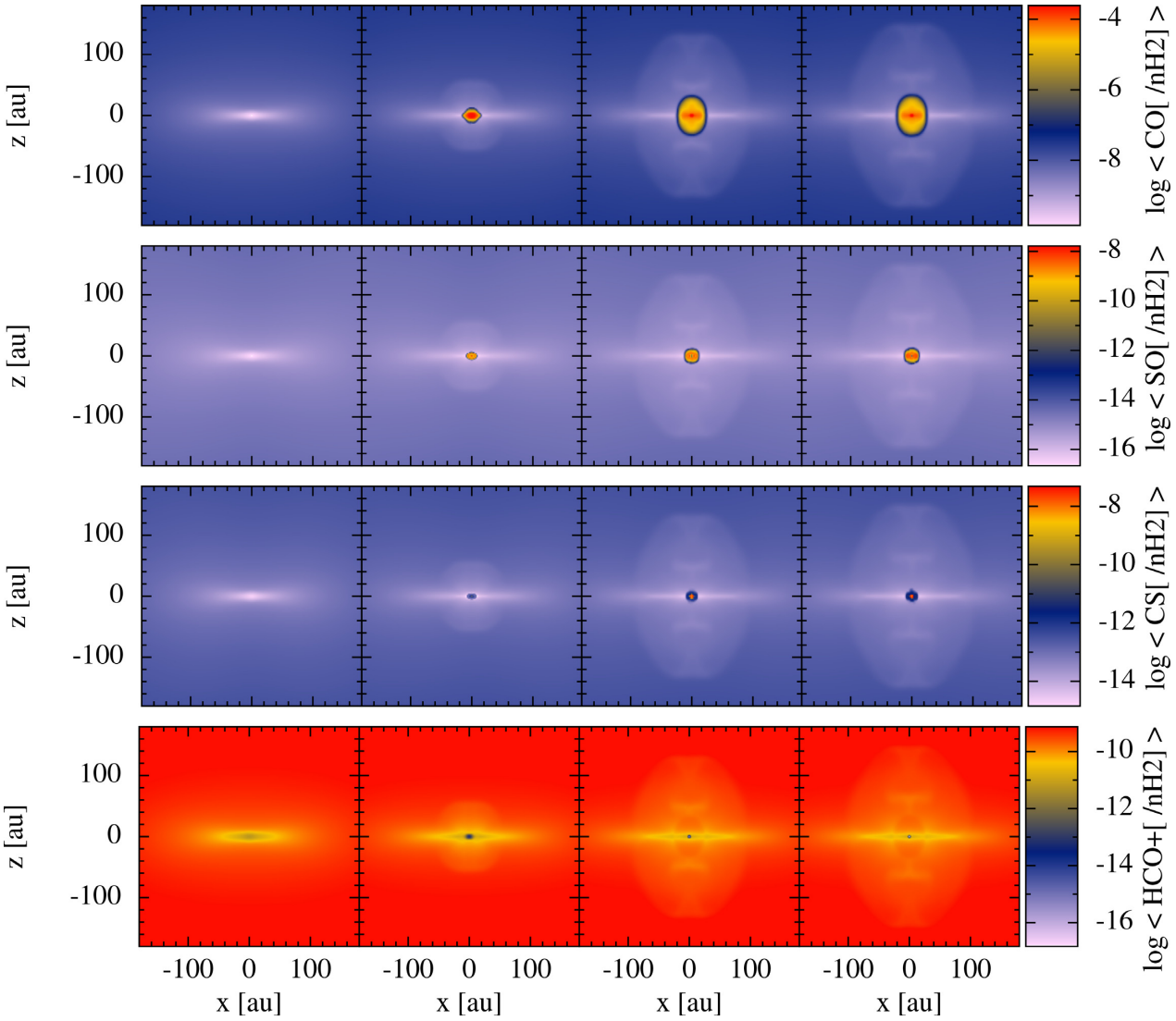

Figure 9. Mass-weighted average abundances (relative to n_{H_2}) of selected species from the MHD model, viewed at $i = 90°$. From left to right, the snapshots are of the first collapse (a), early FHSC (b), late FHSC (d), and just after stellar core formation (g).

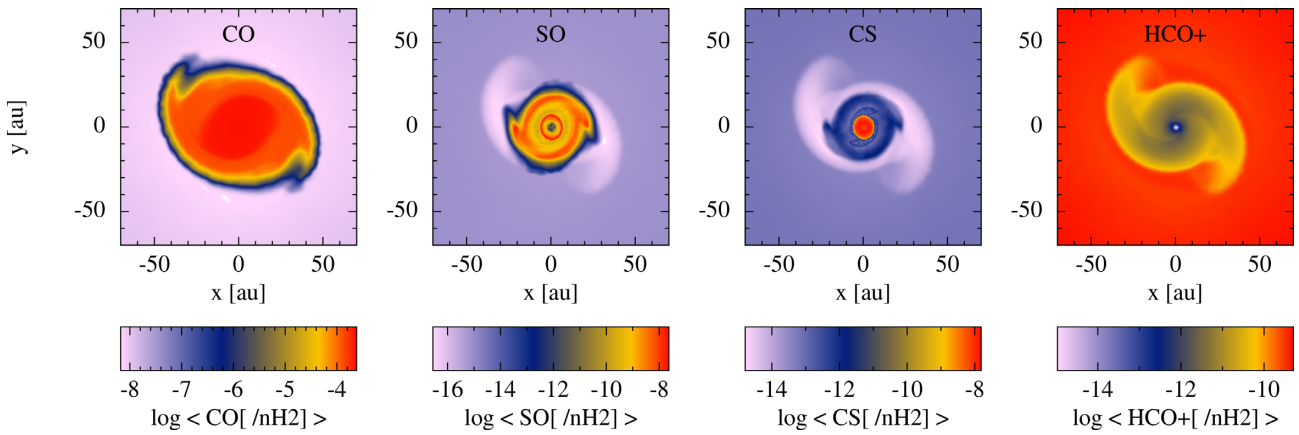

Figure 10. Mass-weighted average abundance relative to n_{H_2} for snapshot (d), late FHSC for CO, SO, CS, and HCO^+, respectively. CO and CS trace the spiral structure of the FHSC and CS traces just the central few au. The HCO^+ abundance is lower in the spiral arms than in the envelope.

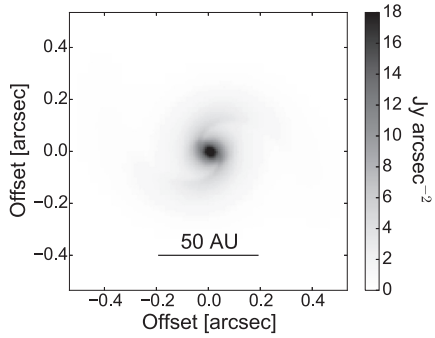

Figure 11. 230 GHz (1.3 mm) continuum image for snapshot (d) from the RHD model. At millimetre wavelengths, the continuum emission is brightest in the centre of the FHSC only and the spiral features are faint. The brightness scale has been capped at 18.0 Jy arcsec^{-2}, but the maximum intensity is 20.2 Jy arcsec^{-2}.

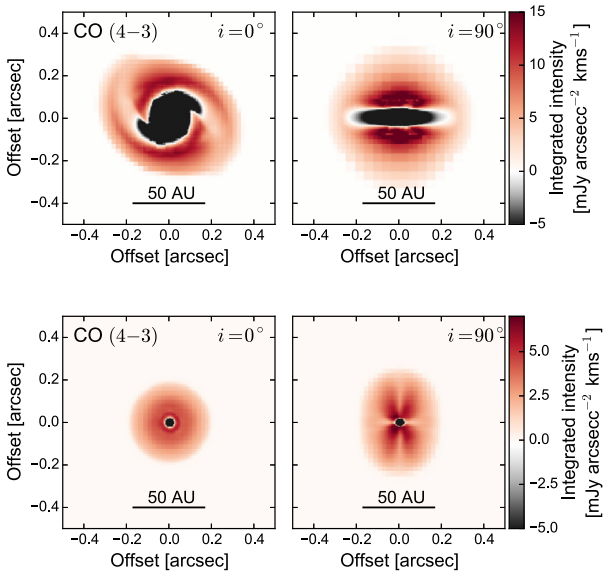

Figure 12. Top: integrated intensity map for late FHSC in the RHD model, after subtracting continuum emission. Bottom: as above but for the MHD model.

3.3.2 CO

From Fig. 10, it is clear that CO traces the region containing the spiral structures in the RHD model. The integrated intensity maps for a snapshot late in the FHSC stage for both the RHD and MHD models are shown in Fig. 12. The CO (4 − 3) line appears to trace the rotational structures present in the RHD model in the face-on direction. The CO (4 − 3) emission reveals two spiral arms but the emission traces the lower density region rather than the spiral features seen in the column density and dust continuum emission (Fig. 11).

There are significant absorption features in the integrated intensity maps where the FHSC continuum emission is absorbed by cooler gas in front of it. This effect is occasionally seen in observations of Class 0 protostars (e.g. Ohashi et al. 2014). The FHSC is smaller in the MHD model so a smaller region is seen in

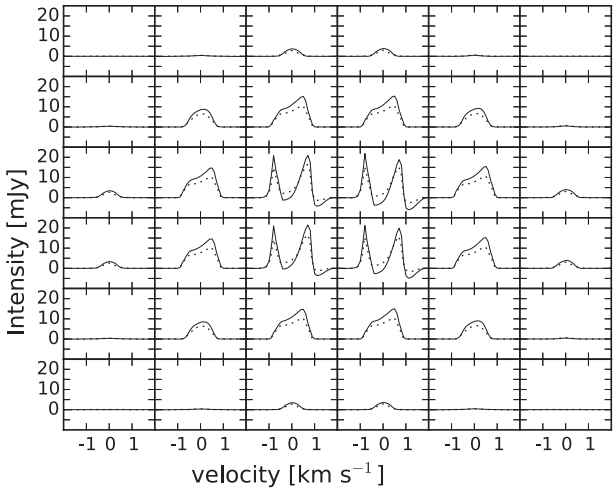

Figure 13. Spectra for CO (4 − 3) (solid lines) and CO (3 − 2) (dotted lines) at $i = 0°$ (face-on) during late FHSC stage (d) of the MHD model. Each panel covers an area of 0.08 × 0.08 arcsec^2. The outflow has recently been launched and is apparent from the double peak.

absorption. The FHSC remains axisymmetric in the MHD model and the integrated intensity map shows a 50 au diameter disc-like structure.

When viewed side-on (inclination $i = 90°$) the dense inner envelope is bright in emission for the RHD model. The outflow structure of the MHD model is apparent in the CO (4 − 3) emission. The CO abundance varies by less than an order of magnitude across the inner region which it traces, indicating that the outflow structure in Fig. 12 (bottom right), is not caused by an increased CO abundance in the outflow. The brighter structures are where the velocities are higher because emission at the higher velocities (>1 km s^{-1}) suffers much less from self-absorption.

The spectra of the late FHSC snapshot from the MHD model in Fig. 13 reveal the kinematics that could be detected at $i = 0°$. The spectrum for each panel was calculated simply by summing the intensities for each pixel in the area of the image covered by the panel. The CO (4 − 3) spectra are brighter, more sharply peaked and have deeper absorption features than the CO (3 − 2) spectra. The line profiles for the snapshot just after stellar core formation are very similar, only slightly brighter.

At $i = 0°$, we are looking down the direction of the outflow. The double-peaked spectra in the four central panels are indicative of the blue- and redshifted components with velocities of ∼1 km s^{-1}. Self-absorption at low velocities also contributes to the central dip. There is a second absorption feature at ∼1 km s^{-1} which is caused by infalling gas directly in front of the FHSC (see Fig. 12, lower right). Outside of the central four panels, the spectra peak at ∼0.7 km s^{-1}. The redshifted emission from the far side outflow is brighter than the emission from the approaching part of the outflow, which causes this asymmetry in the spectra. The nearside emission is self-absorbed because the gas in the outflow, through which the emission propagates, is moving at similar velocities to the emitting gas and this is not the case for the far side emission. The effect of the near side infalling gas on the redshifted outflow CO emission is negligible because the CO abundance is very low in the envelope.

To examine the observable kinematics further we plot the PV cuts for three snapshots during FHSC stages (b–d) and shortly after stellar core formation (g) in Fig. 14 for both the RHD and MHD

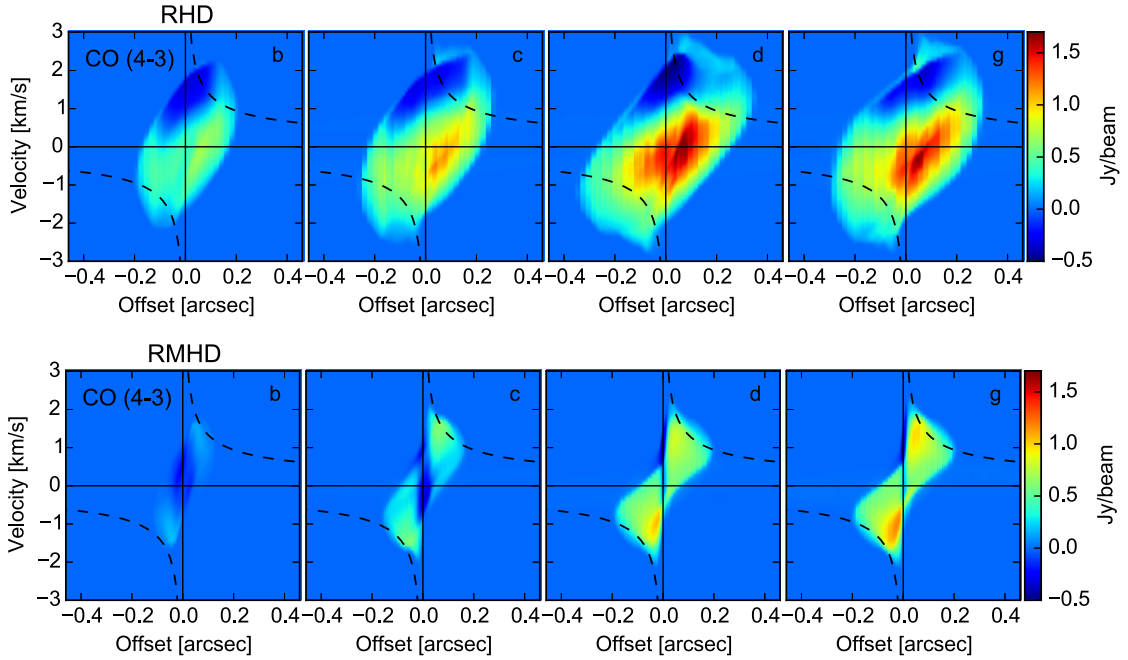

Figure 14. PV diagrams for CO (4−3) (b)–(d) for a series of snapshots of the FHSC and (g) newly formed stellar core viewed at $i = 90°$ inclination. The intensity was summed over an 0.3 arcsec slice centred on the plane of the disc. Dashed lines show the Keplerian rotation profile for a 0.03 $M_\odot$ central protostar.

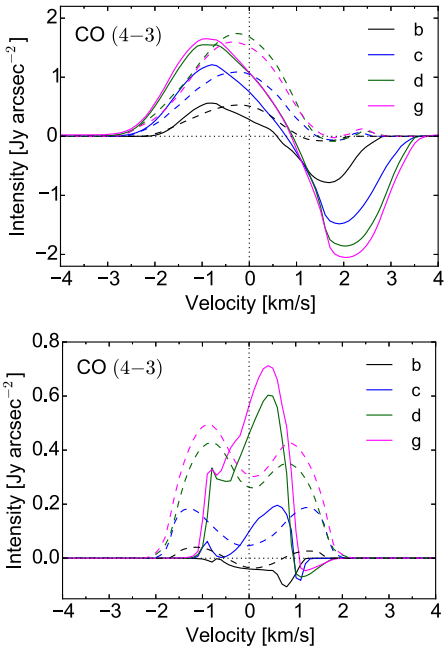

Figure 15. Spectra averaged over a central 0.67 arcsec diameter aperture for RHD model (top) and MHD model (bottom). Solid lines: $i = 0°$ and dashed lines: $i = 90°$. Letters refer to evolutionary stage as defined in Section 3.1.

models. These were constructed from the $i = 90°$ velocity cubes as described in Section 2.4.

The RHD PV diagrams show the characteristics of a rotating infalling structure. The broad absorption feature at ∼1–2 km s^{-1} indicates infalling gas and the velocity increases towards positive offsets because of the contribution of rotation. CO is frozen out just outwards of the spiral shocks at $r \gtrsim 40$ au. The extent of the emission increases as the temperature increases and CO desorbs at increasing radii. There is blueshifted emission to the right hand, receding, side of the object because the gas on the far side has a component in the direction of the observer as it spirals towards the disc. This emission is not self-absorbed due to the velocity difference between the emitting gas and the gas in the disc and near-side envelope through which it passes.

The PV diagram for the MHD model appears to be closer to a Keplerian rotation profile, although this is misleading because there is no rotationally supported disc and gas is spiralling inward through the pseudo-disc. CO is frozen out at $r \gtrsim 20$ au so there is no emission beyond ±0.2 arcsec.

Earlier in the FHSC stage (snapshots b and c) absorption occurs at negative velocities. For snapshot (c), this is likely to be due to absorption in the young outflow. By snapshot (d) absorption occurs only at $v \gtrsim 0.4$ km s^{-1} and is restricted to a very narrow region of <0.04 arcsec. The nature of the CO (4 − 3) absorption feature could provide an indication of the evolutionary stage.

From the evolution of the spectra averaged within a 0.35 arcsec circle shown in Fig. 15, the difference between the RHD and MHD models is even more apparent. The disc in the RHD model is seen almost entirely in absorption against the continuum. Early in the FHSC stage (b), the absorption and emission features are similar in magnitude in the RHD model. The brightness of the emission changes little through to when the stellar core forms but the depth of absorption increases by up to a factor of 3. There is no disc in the MHD model and much of the emission is from the outflow. At (b), the line is entirely in absorption at $i = 0°$. The development of the outflow leads to the emission brightening as gas-phase CO is present in high abundance in a more extended region.

At $i = 90°$, a double-peaked rotation signature is not seen in the RHD model due to the strong absorption at positive velocities by infalling material. The rotating outflow produces a double-peaked

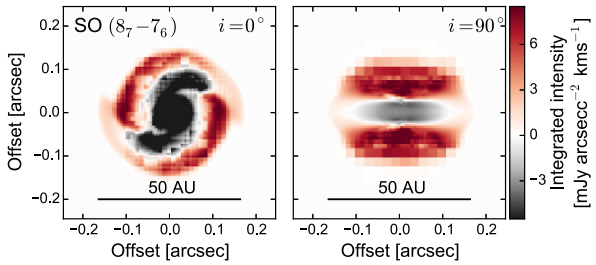

Figure 16. SO integrated intensity maps for the RHD model. We do not show the MHD model because the scale of the emission would be too small to resolve.

spectrum in the MHD model, however, which may be mistaken for a rotating disc (Fig. 15, bottom panel, dashed lines).

Our models assume a turbulent velocity of 0.1 km s^{-1} and we note that a higher value will result in less self-absorption at the systematic velocity of the FHSC as well as slightly broader line widths.

3.3.3 SO

The abundance of SO is $\sim 1 \times 10^{-9}$ within $r < 20$ au in the RHD model and within $r < 10$ au in the MHD model and drops off rapidly outside this region, meaning it is a tracer of the FHSC only in the RHD model (Fig. 10) and of the FHSC and very inner envelope in the MHD model (Fig. 9). At a distance of 150 pc, the region traced in the MHD model is only 0.13 arcsec across so the object will not be well resolved. The abundance of SO is lower in the outer parts of the spiral arms of the RHD model, although SO traces the inner spiral well (Fig. 10). In Fig. 16, the integrated intensity plots reveal significant absorption as seen in CO, which actually traces out the central spiral structure. Emission is limited to a pair of spiral arms at $r \sim 20$ au. At $i = 90°$, we see a 'hamburger' structure with emission from above and below the mid-plane.

SO ($8_7 - 7_6$) spectra for the MHD model are shown in Fig. 17. The line brightens considerably during the early FHSC stage as the temperature increases quickly in the central few au and SO traces an increasing radius. The region traced by SO incorporates only a small section of the outflow where the outflow velocities are <0.5 km s^{-1}. In the same region, the infall and rotation velocities are $\sim$1 km s^{-1}.

The spectra show a clear evolution during FHSC stage. At snapshot (b), the emission is undetectable and the line is symmetrical in absorption. By snapshot (c), the outflow has launched and the line is asymmetrical since it is affected by self-absorption by outflowing gas, giving rise to a redshifted peak. From snapshot (d), there is an absorption feature against the continuum. This becomes less pronounced after the stellar core formation because the density distribution becomes more sharply peaked. The peak becomes more symmetrical as emission from the outflow brightens.

At $i = 90°$, the emission peaks at $\pm$ 1.2 km s^{-1} and the blueshifted peak is brighter, as expected for an infalling, rotating structure. The central absorption dip is skewed to positive velocities due to absorption by infalling material (with a positive recession velocity). The infall velocity is lower here than in the vertical direction due to the added effect of rotation.

Without an outflow, the spectra for the RHD model are quite different. There is a very strong absorption feature from 1.5 to 2.5 km s^{-1}. After stage (c), this does not deepen although the emission peak brightens between snapshots (c) and (d). The $i = 90°$ spectra do not display the characteristic double peak. Looking

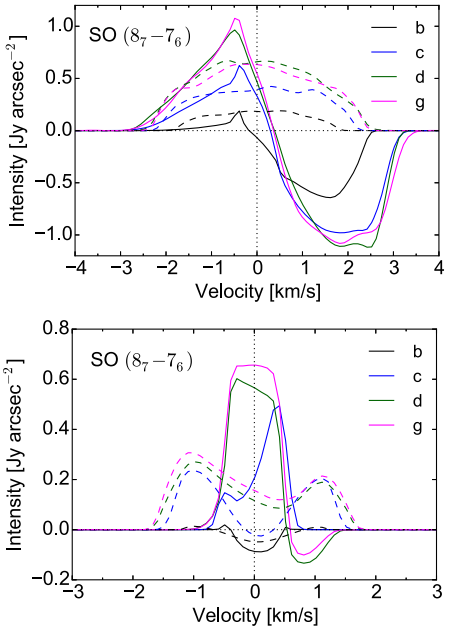

Figure 17. Evolution of the SO ($8_7 - 7_6$) line profile in the MHD model for RHD model (top) and MHD model (bottom). Each spectrum is averaged over pixels within a central 0.35 arcsec (53 au) diameter circular beam. Solid lines: $i = 0°$, and dashed lines: $i = 90°$.

at the integrated intensity images in Fig. 16, we can see that the disc is seen nearly entirely in absorption. Rotation speeds are low above and below the disc where the emission originates and emission at higher velocities is less bright than the low velocity emission from nearer the centre.

3.3.4 CS

The average CS abundance for the late FHSC of the RHD model is presented in the final panel of Fig. 10. The abundance peaks at a few 10^{-8} within $r < 10$ au in a symmetrical distribution and is several orders of magnitude lower elsewhere. We therefore do not expect CS to be useful for tracing rotational structures. The emission will not be well resolved so we consider only the spectra obtained from the total emission within a 0.35 arcsec aperture centred on the FHSC.

Fig. 18 shows the spectra for CS (8 − 7). CS is extremely depleted towards the centre of the cloud core prior to FHSC formation and the abundance soon after formation is still too low to be detectable.

In the MHD model, at $i = 0°$ from snapshot (c) onwards, a sharp peak develops around the CS (8 − 7) line centre and this brightens considerably between the FHSC and stellar core stages. There is an absorption feature at $\sim$1 km s^{-1}. At the frequency of the CS (8 − 7) transition (391.8 GHz), the envelope is optically thin and most of the continuum emission originates within the FHSC or from the very inner envelope near to the FHSC. The optically thin gas directly in front of the FHSC is infalling with a velocity of $\sim$1 km s^{-1} and absorbs the continuum emission. The peaks of the spectra are symmetrical and show no evidence of the outflow. The CS (8 − 7) line brightens between during and beyond the FHSC stage.

At stage (c), mid–FHSC stage, we see symmetrical absorption features around the central peak. The outflow has launched by then with a velocity <1 km s^{-1}. The gas is still relatively dense and there-

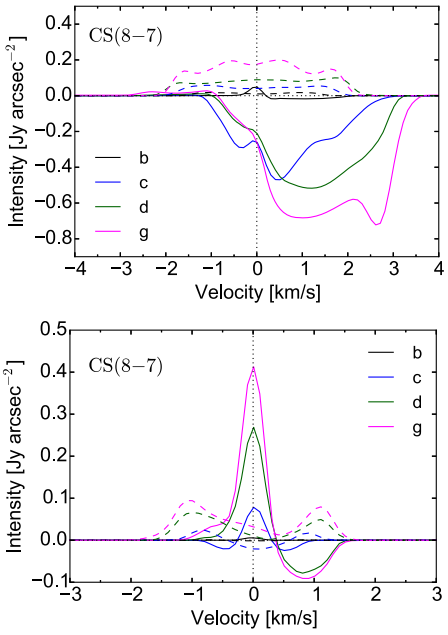

Figure 18. Spectra for CS (8 − 7) obtained from a 0.35 arcsec aperture from the RHD model (top) and MHD model (bottom). Solid lines $i = 0°$; and dashed lines $i = 90°$.

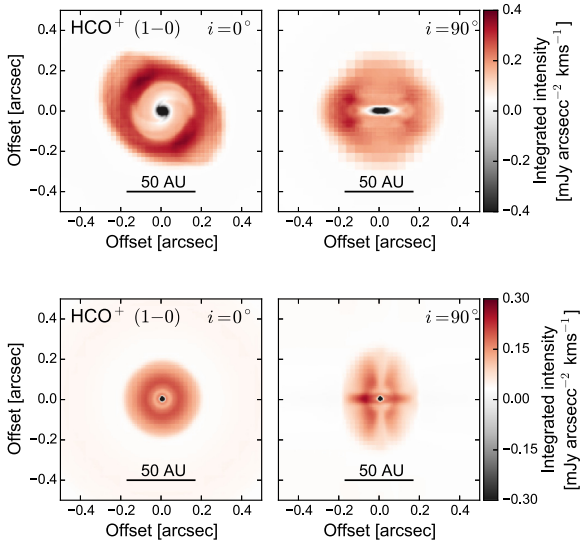

Figure 19. HCO$^+$ (1 − 0) integrated intensity for snapshot (d). Middle: RHD model; and bottom: MHD model.

fore absorbs radiation from the FHSC, but does so predominantly at blueshifted frequencies, since this gas is approaching the observer. Within $\lesssim$5 au from the centre, the gas is infalling at a similar speed to the outflow, which creates the redshifted absorption feature.

At $i = 90°$, the CS (8 − 7) line is double-peaked because of the rotation of the FHSC. The emission is fainter due to the increased optical depth caused by the disc structure such that the emission comes from a slightly larger radius where the temperatures are a little lower. The central dip is deepened by absorption and is skewed to positive velocities due to infall as discussed above.

Spectra from the RHD model show only absorption at $i = 0°$ and little asymmetry at $i = 90°$. Absorption at increasing velocities as the FHSC evolves indicates the increasing infall velocities. In the

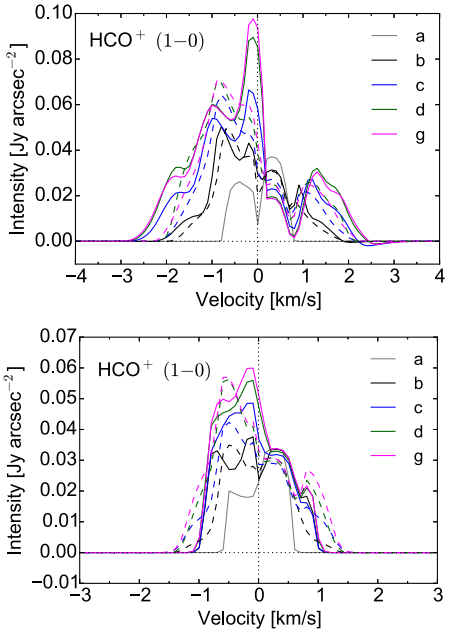

Figure 20. HCO$^+$ (1 − 0) spectra for RHD model (top) and MHD model (bottom) within a 0.67 arcsec aperture. N.B. These use a grid of 5350 au rather than the 400 au grid used for the other species.

ideal MHD model, the additional support from the magnetic field reduces infall speeds so the spectra reveal a narrower velocity range.

3.3.5 *HCO$^+$*

The abundance of HCO$^+$ is highest in the regions of the lowest density and it is depleted in the FHSC and disc (Fig. 10). The integrated intensity map for the RHD model (Fig. 19, top left) shows an asymmetrical ring with a central hole. This feature is commonly observed in HCO$^+$ near protostellar sources, albeit on scales of hundreds of au rather than tens of au (e.g. Jørgensen et al. 2013). Only the inner envelope at $r \sim$ 30–50 au is warm enough to produce significant HCO$^+$ (1 − 0) emission and within the disc the HCO$^+$ emission is much fainter, primarily due to depletion at $r \lesssim 15$ au (see Figs 5–9). At $i = 90°$, the approaching (left) side is visibly brighter in both models. This is a well-known phenomenon for rotating, infalling envelopes observed in an optically thin line.

The emission in the MHD model also has the appearance of a disc and a smaller region is traced. What we see is not just the pseudo-disc but also the conical outflow from above. At $i = 90°$, the emission is also less extended than in the RHD model, despite the presence of an outflow. Here, the HCO$^+$ line traces the pseudo-disc and outflow and there are brighter structures in the outflow like those seen in the CO emission.

The spectra for both models are double-peaked at $i = 0°$ (Fig. 20). For the RHD model, this is due to the combination of infall motions and the self-absorption dip at low velocities. The spectra for the MHD model have similar features but the infall speeds are lower. The emission from the outflow at $i = 0°$ in the MHD model at $\sim$−0.5 km s^{-1} reduces the depth of the dip between the central and blueshifted peaks from snapshot (c) onwards.

Before FHSC formation, there is no central emission peak at the line centre. This central peak brightens as the core evolves and, from late in the FHSC stage, it is brighter than the blueshifted peak. This is true for both RHD and MHD models and provides a possible

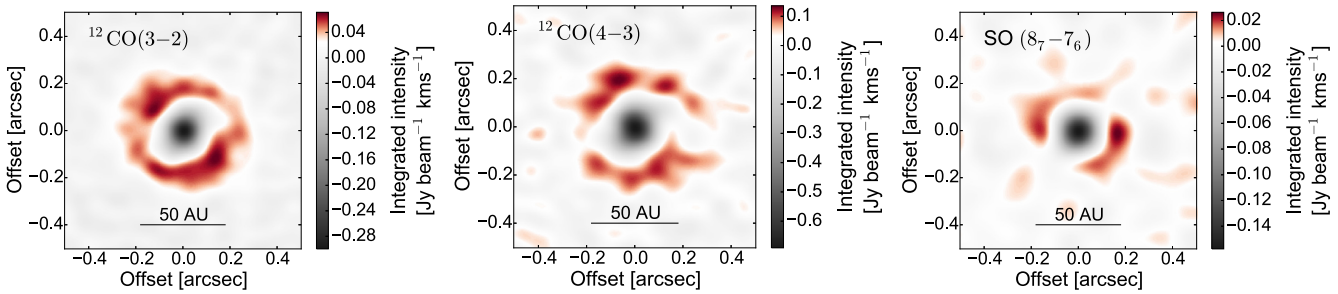

Figure 21. Synthetic ALMA observations of snapshot (d) of the RHD model in the face-on direction all with pwv = 0.8, left to right: CO (3 − 2) 4 h total time, ALMA out16 configuration giving 0.08 × 0.1 arcsec beam; CO (4 − 3), ALMA out14 configuration giving 0.11 × 0.09 arcsec beam, 8 h total integration; SO ($8_7 - 7_6$), and ALMA out14 configuration giving 0.15 × 0.12 arcsec beam, 8 h total time.

indication of the presence of an FHSC. The relative strengths of the line centre and red- and blueshifted peaks do depend on the aperture over which the spectra are averaged. The HCO^+ abundance is extremely low in the centre so this emission at the line centre is not simply coming from the FHSC. In the RHD model, the HCO^+ abundance increases within a shell between ∼20–30 au (cf. Figs 5 and 6). This coincides with the outer regions of the disc-shaped FHSC, which strongly suggests that we are seeing the build up of material in the mid-plane. This feature is weaker in the MHD model (cf. Figs 7 and 8), which makes sense because gas is infalling along the mid-plane, i.e. the radial velocity = 0 for $i = 0$, but no disc forms so the density is lower.

3.4 Detectability with ALMA

In this section, we examine the observability of features identified in the previous section by simulating ALMA observations. For all synthetic ALMA observations, we assume a realistic precipitable water vapour (pwv) = 0.8 mm, unless otherwise stated, and use Briggs weighting. Simulated ALMA integrated intensity maps are presented in Fig. 21 and spectra in Figs 22 and 23.

The asymmetric CO (4 − 3) emission is discernible after a total on source time of 8 hours with the `out14` configuration (beam size 0.11 × 0.09 arcsec) (Fig. 21, centre panel). The absorption at the centre is very prominent and certainly detectable with a shorter integration. No additional detail is gained by using a smaller beam due to the increased noise. The CO (3 − 2) line (Fig. 21, left-hand panel) is brighter and it is possible to obtain a similar level of detail with the `out16` configuration (0.1 × 0.08 arcsec beam) with a far shorter 4 h integration. Emission from the spiral arms clearly traces the asymmetric central region where the CO is seen in absorption. The CO (3 − 2) line is more likely to be contaminated by the foreground cloud so it is encouraging that the detection of non-axisymmetric structure is achievable in the higher (4 − 3) transition. SO ($8_7 - 7_6$) is also detectable (Fig. 21, right-hand panel) and traces the spiral arms clearly with a total integration of 8 h and the `out14` configuration (0.09 × 0.1 arcsec beam).

The CO (4 − 3) spectrum in Fig. 13 showed a double-peaked feature, characteristic of the outflow, and we find that it should be possible to detect this with ALMA. In Fig. 22 (top), the panels each cover a larger area due to the lower resolution of the convolved image but the feature is present in the central panels after a total on source time of 8 h. A high resolution of ∼0.1 arcsec is needed to detect the double-peak, otherwise it is hidden by low velocity emission from the pseudo-disc.

Many of the observed candidate FHSCs have accompanying detections of slow outflows. In Section 3.3.2, we showed that CO

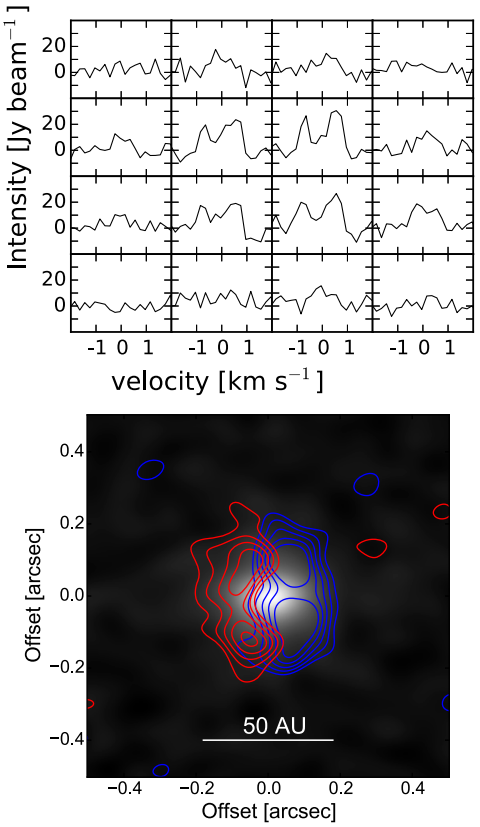

Figure 22. Synthetic ALMA observations of the MHD model snapshot (d) in CO (4 − 3). Top: face-on direction, total integration time of 8 h, pwv = 0.8 mm and 0.1 × 0.09 arcsec beam. Each panel is 0.12 arcsec across. Bottom: red and blue contours show integrated intensity in the edge-on direction from 0 to 4 km s^{-1} and −4 to 0 km s^{-1}, respectively. Continuum is shown in greyscale. A total integration of 6 h, beam size 0.1 × 0.09 arcsec and pwv = 0.5 mm.

emission should trace the inner regions of the outflow. However, in the simulated ALMA observation in Fig. 22 (bottom panel), there is no clear outflow structure either in the continuum or CO (4 − 3) line emission. The line emission reveals red- and blueshifted lobes, indicative of the rotation of the outflow. The rotation velocities are comparable to, or higher than, the outflow velocities. Even at low inclinations, the outflow motions were not detectable but rotation should be observable with ALMA with a 6 h integration.

The SO ($8_7 - 7_6$) transition revealed a shift in the line centre and the development of an absorption feature between snapshots (c) and

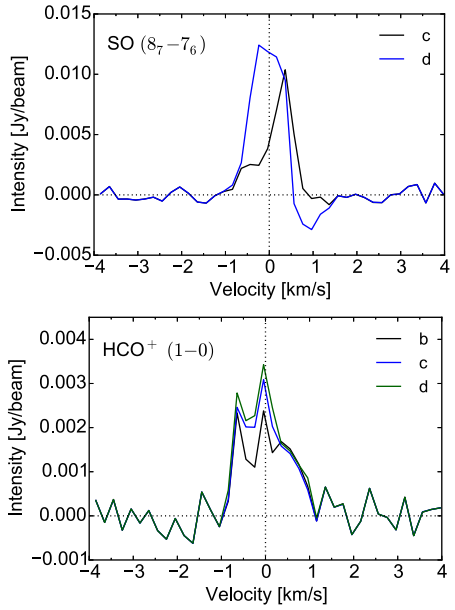

Figure 23. Synthetic ALMA spectra of the MHD model in the face-on direction. Top: SO ($8_7 - 7_6$), 8 h total integration, out14 configuration. It is possible to distinguish spectra early and late in FHSC stage at $i = 0°$ as the outflow develops. Bottom: MHD model HCO$^+$ (1–0), 8 h total integration, 0.21 × 0.25 arcsec beam. As the FHSC grows emission increases at the line centre and becomes brighter than the blue peak and this is still discernible in the synthetic interferometric spectra.

(d). This difference is still clear in the simulated ALMA observation (Fig. 23, upper panel) and may provide a method for distinguishing a source mid-way through FHSC stage from a more evolved object. In HCO$^+$ too (Fig. 23, lower panel), the difference between the spectra of snapshots (b) and (c) is clear although somewhat more subtle.

CS emission was found to be indistinguishable from noise even with an 8 h integration with pwv =0.5 mm for both the (8 − 7) and (2 − 1) transitions from the MHD model. The CS (8 − 7) line only became detectable for the last snapshot (g) with excellent observing conditions of pwv = 0.2 mm and an 8 h integration with the `out20` configuration.

4 DISCUSSION

4.1 Chemical abundances

Abundances of chemical species that form primarily on the surface of dust grains are highly underestimated and so we do not simulate observations for them. We now compare the abundances of several species presented in this paper with observed values, bearing in mind that the observed values were measured for dense starless cores. We will later compare our chemical abundances to the results of other simulations in Section 4.5.

The calculated initial abundance of CO is 1×10^{-4} which is similar to the measured CO abundances in TMC-1 (1.7×10^{-4}) and L134N (8.7×10^{-5}) (Dickens et al. 2000; Agúndez & Wakelam 2013). As the core collapses and the density increases, the CO freezes out and the abundance is lower than TMC-1 and L134N, which is to be expected as the density exceeds that of L134N ($n_{H2} \approx 2 \times 10^4$ cm^{-3} which corresponds to 8×10^{-20} g cm^{-3}, Dickens et al. 2000) and TMC-1 ($n_{H2} \approx 8 \times 10^4$ cm^{-3} which corresponds to 3×10^{-20} g cm^{-3}, Pratap et al. 1997).

The initial abundance of HCO$^+$ is 7×10^{-9} which is similar to the measured abundance of 7.9×10^{-9} in L134N (Dickens et al. 2000) and a little lower than the value of 9.3×10^{-9} found for TMC-1 (Pratap et al. 1997).

The initial abundance of CS (2×10^{-8}) is an order of magnitude greater than that observed in TMC-1 (Pratap et al. 1997) and the KIDA network overestimates the CS abundance for $t < 10^6$ yr. CS freezes out in the collapsing dense core and only exceeds 10^{-10} in the central few au. Observations of the FHSC candidate Cha-MMS1 (Tsitali et al. 2013) find a CS abundance of 2.5×10^{-9} at a radius of 8000 au, which is consistent with our calculations if extrapolated to this radius.

The SO abundance is significantly lower by ∼4 orders of magnitude initially than observed in TMC-1 and L134N. The initial abundance of NH_3 is initially 10 times lower than observed in TMC-1 and L134N and reaches a few 10^{-9} in the core.

4.2 Spatially resolved structures

The spiral structure that develops in the RHD model should easily be spatially resolved in dust continuum observations. Indeed, there are now several examples of such structures observed in discs (e.g. Grady et al. 2013; Pérez et al. 2016; Stolker et al. 2016). We can examine whether the rotational or outflow structures are more prominent in line observations than the continuum after modelling the chemical evolution and the line emission.

The spiral structure remains more easily observed in continuum emission on scales of ∼20 au. This is, in part, because the lines of species that trace the FHSC are seen in absorption against the continuum across most of the FHSC. SO ($8_7 - 7_6$), CO (3 − 2), and CO (4 − 3) do however trace the spiral structure on scales of 50–60 au where the continuum emission is much fainter.

While HCO$^+$ and CO emission traces the outflow, the extent is very small at a representative distance of 150 pc. HCO$^+$ emission is also very faint. Any structure will be difficult to distinguish from noise even with an on source time of 8 hours.

Observations of CO (4 − 3) and SO ($8_7 - 7_6$) lines could be used to supplement continuum observations of rotating candidate FHSCs at low inclinations to provide evidence of rotational structures. For the MHD model here, it looks unlikely that the outflow will be detectable in HCO$^+$ line emission maps. The outflow is not well defined in the simulated ALMA integrated intensity map, but red and blue lobes are just detectable within 8 h in CO(4 − 3) (see Fig. 22, lower panel).

4.3 Kinematics

Currently, the outflow velocity is one of the factors considered when classifying a faint, young source as a candidate FHSC. FHSC outflows are expected to be wide and to have velocities of a few km s^{-1} (e.g. Tomisaka 2002; Machida et al. 2008; Bate et al. 2014; Lewis & Bate 2017; Wurster et al. 2018). Some sources identified as candidate FHSCs have later been reclassified when further observations revealed a collimated outflow, faster than ∼10 km s^{-1} once inclination effects were considered (e.g. Per-Bolo 58, Dunham et al. 2006, and B1-bS, Gerin et al. 2015). During the relatively short lifetime of the FHSC, the extent of the outflow is only a few 100 au and infall velocities are comparable to outflow velocities so it is questionable whether the FHSC outflow would be detectable.

Of the species considered here, only CO spectra clearly show the signature of the outflow. This is because the CO abundance is much higher in the outflow out to ∼30 au above the mid-plane than in the envelope. However, the outflow velocities are so slow that once we consider a moderate inclination the outflow velocity component becomes negligible in comparison to the rotational and, in reality, turbulent motions. The contribution of the outflow to the $HCO^+(1-0)$ spectrum is less clear. This line is optically thin and still dominated by infall due to the higher relative abundance in the envelope than the denser central regions.

The different chemical species trace infall on different scales. Infall is apparent in the optically thick lines as redshifted absorption against the continuum. Species such as CS and SO trace regions within the FHSC and a few au above the mid-plane and reveal infall onto the FHSC. As expected, HCO^+ traces larger scale infall onto the disc.

Most of these species display the double-peaked rotation signature in the spectra viewed from edge-on. This is not true of SO, CS, or CO from the RHD model, however. In both CO and SO, the disc is seen in absorption. SO traces a smaller radius than CO but most of the central part of the disc is optically thick. The SO emission comes from essentially a narrow ring offset from the mid-plane. The resulting spectrum is then missing the double peak. The same is true for CS but on a smaller scale. We emphasize that the rotation signatures appear to be stronger for the MHD model which does not have a rotationally supported disc but has a rotating outflow.

4.4 Observing with ALMA

Many species that may in theory distinguish features associated with the FHSC, including CS, are likely to be too faint to detect, even with ALMA. Temperatures are still very low in much of the object so abundances of ISM species are depleted with respect to the surrounding envelope. In addition, outflow and disc structures are still relatively compact (hundreds and tens of au, respectively). Efforts to identify an FHSC should therefore concentrate on just the most abundant species.

Although these structures are still compact, the resolution is a less important consideration than minimizing the noise. We find the optimum resolution is 0.08–0.1 arcsec for detecting rotational structures at 150 pc. With a synthesized beam of 0.1 arcsec, the largest recoverable scale is ∼1.5 arcsec which means that emission from the inner envelope should be acceptably recovered. Observations were synthesized here with a realistic value for pwv = 0.8 mm. For worse observing conditions, the FHSC structures are very likely to be indistinguishable from noise. In order to detect the outflow spatially in CO, pwv ≤0.5 mm is necessary. An on-source time of 8 h is required for the lines modelled here. Only CO (3 − 2) is feasible with a shorter, 4 h, integration.

4.5 Comparison to other work

There have been only a few prior attempts to model chemistry of collapsing dense cores that we know of, some from analytical density and temperature structures and some from hydrodynamical models. We compare to the following work, where possible, since not every paper includes every chemical species. Aikawa et al. (2008) calculated chemical abundances for a 1D frequency-dependent radiation hydrodynamical model of a collapsing core. The chemical calculations included gas-phase and grain surface reactions and assumed low metal elemental abundances. van Weeren, Brinch & Hogerheijde (2009) performed similar calculations but from 2D hydrodynamical models, allowing the effects of a disc structure to be explored. The chemical evolution was followed for 700 tracer particles by calculating gas-phase, gas-grain, and grain surface reactions. Furuya et al. (2012) used a 3D RMHD model of a collapsing 1 $M_\odot$ cloud, calculating chemistry for 10^5 tracer particles. Gas-phase and grain surface reactions were included. Hincelin et al. (2016) specifically set out to look for chemical differences between different components of the core in 3D. They performed several RMHD simulations of a collapsing 1 $M_\odot$ cloud and calculated the chemical evolution of 10^6 tracer particles with gas-phase and grain surface reactions. Dzyurkevich et al. (2016) used a reduced network of mainly gas-grain H-C-O chemistry to calculate abundances at the same time as calculating the dynamical evolution of the collapse of a dense core. Maret, Bergin & Tafalla (2013) attempted to model the chemistry and two line profiles to compare to two observed pre-stellar cores. They took an analytical density profile which did not vary in time since they did not seek to model a collapsing core but these results are useful to compare with the abundances in the envelope here. The chemical model included gas-phase and gas-grain reactions. We note that the above papers quote abundances relative to the total density of hydrogen nuclei and we account for this in the comparison.

The highest abundances of CO that we obtained during the collapse of the pre-stellar core are approximately a factor of 2 higher than those reported by Furuya et al. (2012), which used a ≈ 50 per cent lower elemental C^+ abundance. The envelope abundance of CO was a few $\times\ 10^{-7}$ which is similar to the values of Hincelin et al. (2016) and Furuya et al. (2012) and to the abundance from the fiducial single-sized dust grain model (S1) of Dzyurkevich et al. (2016) at ∼2000 au.

In the envelope, we find an HCO^+ abundance of a few $\times\ 10^{-9}$, which is similar to that of van Weeren et al. (2009) and Dzyurkevich et al. (2016) at ∼6000 au in their models. This abundance is a little higher than that found for similar radii by Maret et al. (2013) and Aikawa et al. (2008).

Abundances of CS in the FHSC and envelope have previously been calculated to be a few $\times\ 10^{-11}$ (van Weeren et al. 2009; Hincelin et al. 2016) or as high as 10^{-8} (Aikawa et al. 2008). Between these regions CS is very highly depleted. We find the abundance in the centre to be a few $\times\ 10^{-9}$ and a few $\times\ 10^{-12}$ in the outer envelope.

The abundance of NH_3 is lower than the central values of a few 10^{-6} to a few 10^{-5} reported by others (Aikawa et al. 2008; van Weeren et al. 2009; Hincelin et al. 2016). The initial abundance of N_2H^+ agrees well with the envelope abundances of van Weeren et al. (2009) and Hincelin et al. (2016). The abundance in the centre is a few 10^{-20} as was found by Hincelin et al. (2016) but we find the abundance in the disc and pseudo-disc to be far lower than the abundances they report for those regions.

Synthetic CS spectra were presented by Tomisaka & Tomida (2011) and these are qualitatively very different to those here, but their models assumed a constant CS abundance of $4\ \times\ 10^{-9}$ throughout whereas we expect CS to be depleted as the pre-stellar core collapses. It is not returned to the gas phase in the envelope until some time after the protostar has formed (see also Aikawa et al. 2008 for a study of the chemical changes that occur as the protostellar core warms up). We find that the CS sublimation radius extends to ∼10–15 au in the MHD model (Figs 5 and 6) so does not trace the gas kinematics. In the RHD model, the CS sublimation radius extends to 20–30 au (Figs 7 and 8) because the FHSC is larger due to the greater rotational support. In addition, because of

the freeze out, the CS (8 − 7) emission is faint, and likely to be undetectable during much of the FHSC phase.

Hincelin et al. (2016) find that species such as CS and HCO^+ may be useful for distinguishing the envelope from the outflow and pseudo-disc. We also find a difference in abundance between the envelope and these components but for CS the spectrum is still dominated by the central few au where the abundance of CS and temperature are much higher. For HCO^+, the decrease in abundance in the disc and outflow is offset by the enhanced density and temperature such that the outflow and pseudo-disc are brighter than the envelope in emission maps. We agree with their conclusion that the chemistry of the envelope alone cannot distinguish between FHSC formation models. The temperature profile of the envelope changes very little and changes in the composition of the envelope are likely to occur only on longer time-scales. Nevertheless, the spectra are very sensitive to the distribution of chemical species so chemical evolution should certainly be taken into account when simulating molecular line observations.

4.6 Determining evolutionary stage

The main objective of modelling the chemistry and synthetic observations of the FHSC is to determine how to distinguish it from 'empty' pre-stellar cores and from very young protostars. The abundances of CS and SO are extremely low before FHSC formation and the SO ($8_7 - 7_6$) line becomes detectable mid-way through the FHSC stage. CS (8 − 7) remains undetectable with 8 h integration with ALMA throughout FHSC stage and will still be close to the detection limit after stellar core formation, even in the best observing conditions. A detection of CS at subarcsecond scales would preclude a source from being an FHSC.

Changes in the shape of the SO ($8_7 - 7_6$) spectrum at low inclinations when the outflow is launched should be detectable with ALMA. The central peak of HCO^+ (1 − 0) becomes brighter than the blueshifted peak late in the FHSC stage, offering another possible indicator of evolutionary stage.

Factors other than age cause considerable variation in the properties of the spectra. For this reason, it is probably not possible to provide generic criteria to distinguish an FHSC from a stellar core. The positive identification of the FHSC is going to require specific modelling of individual sources based on observationally derived morphology, magnetic field, and dust properties to determine the spectra expected from those specific conditions.

4.7 Comparison to observations of candidate FHSCs

There are a few published observations of candidate FHSCs with better than 1000 au resolution. We now consider whether these sources are genuinely in the FHSC stage in light of this work and also from the SED fitting of Young et al. (2018).

CS (2 − 1) and CS (5 − 4) transitions have been detected at the FHSC candidate Chamaeleon-MMS1 (Tsitali et al. 2013). We do not expect there to be detectable CS emission from the FHSC and what is detected here is mostly emission from the surrounding envelope since the beam size (24.9 arcsec) is much larger than our models. It would be informative to obtain interferometric observations of CS emission with a smaller beam to determine its source. The abundance of CS increases quickly within $r < 50$ au after stellar core formation, during which time the extent of the outflow would not have increased significantly. The stellar core outflow is expected to launch very quickly after formation unless the magnetic field is weak or misaligned. While it is unlikely that Cha-MMS1 is an FHSC, it is also unlikely to have evolved far beyond stellar core formation. Further observations suggest rotational motions and an absence of shocks, which also points to it being a very young object. The results of previous SED fitting indicated too that Cha-MMS1 is more likely to be a very young protostar than an FHSC (Young et al. 2018).

Another candidate is L1451-mm where a slow, poorly collimated outflow was detected in CO (2 − 1) (Pineda et al. 2011; Tobin et al. 2015). We find that CO should indeed trace the outflow although in the synthetic observations the velocity channels trace the rotational motions of the outflow. The observed CO extends for several hundred au which is a far larger region than we would expect, unless the lifetime of the FHSC is longer than expected.

Two candidate FHSCs in Ophiuchus presented by Friesen et al. (2018) are also consistent with the results here. Blue- and redshifted CO (2 − 1) emission was detected at SM1N without a clear outflow morphology. This is what we find from simulated ALMA observations: the FHSC outflow has a small extent and once the image was convolved with the ALMA beam and noise was added we did not see a clear outflow structure. N6-mm also appears to have a compact and broad outflow. No absorption against the continuum was observed at either source but this is not expected in CO from the MHD model.

The SED of CB17-MMS1 is consistent with a young FHSC (Young et al. 2018). There is also a rather confusing structure seen in CO (2 − 1) emission thought to be associated with the source (Chen et al. 2012). If this is tracing an outflow then the extent is probably too great for an FHSC since we expect only the central part of the outflow to be detectable where temperatures are high enough for CO to desorb from dust grains.

B1-bN is another FHSC candidate that has been observed several times now. Previous SED modelling indicated that the source is consistent with an FHSC but only if it has a substantial disc and is viewed at a near side-on inclination (Young et al. 2018). An outflow has been detected in CO (2 − 1) (Hirano & Liu 2014), H_2CO ($2_{02} - 1_{01}$), and several CH_3OH (3 − 2) lines (Gerin et al. 2015). This outflow is thought to extend to ≈1000 au (see table 3 of Gerin et al. 2015). We find that CO only traces the inner few tens of au of the outflow and H_2CO and CH_3OH are unlikely to trace a much more extended region than CO. Therefore, it is difficult to explain this observation as an FHSC outflow with such a large extent. Gerin et al. (2015) also point out that the outflow is not aligned with the magnetic field which means it is possible that the source is a slightly more evolved object but with a shorter and less well-collimated outflow than might be expected for its age.

4.8 Limitations

The chemical network used here omitted grain-surface reactions and we therefore excluded species known to be governed by surface reactions. Species such as formaldehyde and methanol are very likely to be good tracers of the outflow so it is worth modelling observations of these in future. The chemical network we have used is valid between 10–800 K and is extrapolated in the inner 1 au after late FHSC stage. While this is unlikely to affect the results here which concern larger scales, the calculated abundances in the centre of the FHSC may be different when additional reactions and correct rates are considered.

In this paper, we used two extreme models: one which forms a disc and another which forms an outflow and pseudo-disc. Other initial conditions will result in a combination of these structures.

Specific modelling is therefore required to compare with particular sources in detail.

5 CONCLUSIONS

We have presented synthetic CO, CS, SO, and HCO^+ observations produced from hydrodynamical and chemical modelling of the formation and evolution of the FHSC. We showed that rotational structures should be detectable by ALMA in CO (4 − 3) and SO (8_7 − 7_6) transitions in realistic observing conditions. CO emission did not reveal the outflow morphology in simulated ALMA maps but red and blue lobes caused by rotation, rather than outflowing motions, were detectable.

Regarding determining the evolutionary stage, we find changes in SO and HCO^+ spectra as the FHSC develops when viewed at a low inclination. We find that CS is difficult to detect during the FHSC stage with a reasonable integration time and observing conditions with ALMA. This means that candidate FHSCs with CS detections on subarcsecond scales (i.e. without significant contribution from the envelope) are unlikely to be FHSCs; they are likely to be more evolved.

FHSC structures are still very compact and most chemical species are frozen out in much of the inner envelope. Although chemical evolution alone is unlikely to provide a diagnostic of the FHSC, synthetic molecular line observations should account for chemical evolution. Using constant spatial abundances is likely to lead to incorrect synthetic observations.

Finally, we compare these results with selected candidate FHSCs. We rule out B1-bN due to the detection of an outflow which extends ∼1000 au. Cha-MMS1 is more likely to be a very young protostar but we cannot rule it out completely because there is no reported detection of an outflow and existing observations resolve regions no smaller than 1000 au. L1451-mm is unlikely to be in FHSC stage because the extent of the observed outflow is greater than we would expect. Similarly, if the observed CO emission near CB17-MMS1 is tracing an outflow driven by the source then it is too extended to be driven by an FHSC. This leaves Oph A SM1N and N6-mm as the most promising sources to follow up.

Identifying the FHSC in nature will require interferometric observations of lines such as CO (4 − 3) and SO (8_7 − 7_6) with a spatial resolution ∼0.05 arcsec and a velocity resolution of 0.2 km s^{-1} to detect structures on the scale of a few tens of au. Detection of these lines should be achievable within an 8 h integration with ALMA.

ACKNOWLEDGEMENTS

We thank Jennifer Hatchell and Stefan Kraus for helpful discussions regarding the interpretation of observations and interferometry. We are also grateful to Tom Douglas for his advice on processing data files and to Catherine Walsh for a useful conversation about chemical networks. We also thank the anonymous referee for suggesting that we compare both the KIDA 2011 and 2014 chemical networks.

This research made use of Astropy,[2] a community-developed core PYTHON package for Astronomy (Astropy Collaboration et al. 2013; Price-Whelan et al. 2018). Some figures were produced using the publicly available SPLASH visualization software (Price 2007).

This work was supported by the European Research Council under the European Commission's Seventh Framework Programme (FP7/2007-2013 Grant Agreement No. 339248). Calculations discussed in this paper were performed on the University of Exeter Supercomputer, a DiRAC Facility jointly funded by the Science & Technology Facilities Council (STFC), the Large Facilities Capital Fund of the Department for Business, Innovation and Skills (BIS), and the University of Exeter. This work made use of the Cambridge Service for Data Driven Discovery (CSD3), part of which is operated by the University of Cambridge Research Computing on behalf of the STFC DiRAC HPC Facility (www.dirac.ac.uk). The DiRAC component of CSD3 was funded by the Department for Business, Energy & Industrial Strategy (BEIS) capital funding via STFC capital grants ST/P002307/1 and ST/R002452/1 and STFC operations grant ST/R00689X/1. This work also used the DiRAC Complexity system and the DiRAC Data Intensive service, operated by the University of Leicester IT Services, which forms part of the STFC DiRAC HPC Facility. The Complexity system was funded by BIS National E-Infrastructure capital grant ST/K000373/1 and STFC DiRAC Operations grant ST/K0003259/1. The Data Intensive service is funded by BEIS capital funding via STFC capital grants ST/K000373/1 and ST/R002363/1 and STFC DiRAC Operations grant ST/R001014/1. DiRAC is part of the National e-Infrastructure.

[2] http://www.astropy.org

REFERENCES

Agúndez M., Wakelam V., 2013, Chem. Rev., 113, 8710
Aikawa Y., Wakelam V., Garrod R. T., Herbst E., 2008, ApJ, 674, 984
Astropy Collaboration et al., 2013, A&A, 558, A33
Banerjee R., Pudritz R. E., 2006, ApJ, 641, 949
Bate M. R., 1998, ApJ, 508, L95
Bate M. R., 2011, MNRAS, 417, 2036
Bate M. R., Keto E. R., 2015, MNRAS, 449, 2643
Bate M. R., Bonnell I. A., Price N. M., 1995, MNRAS, 277, 362
Bate M. R., Tricco T. S., Price D. J., 2014, MNRAS, 437, 77
Benz W., 1990, in Buchler J. R., ed., Proc. NATO Advanced Research Workshop on The Numerical Modelling of Nonlinear Stellar Pulsations Problems and Prospects, held in Les Arcs, France, March 20–24, 1986. Kluwer Academic Publishers, Dordrecht, The Netherlands, p. 269
Chen X., Arce H. G., Dunham M. M., Zhang Q., Bourke T. L., Launhardt R., Schmalzl M., Henning T., 2012, ApJ, 751, 89
Commerçon B., Launhardt R., Dullemond C., Henning T., 2012, A&A, 545,
Commerçon B., Levrier F., Maury A. J., Henning T., Launhardt R., 2012, A&A, 548, A39
Dickens J. E., Irvine W. M., Snell R. L., Bergin E. A., Schloerb F. P., Pratap P., Miralles M. P., 2000, ApJ, 542, 870
Draine B. T., Lee H. M., 1984, ApJ, 285, 89
Dunham M. M. et al., 2006, ApJ, 651, 945
Dzyurkevich N., Commerçon B., Lesaffre P., Semenov D., 2016, preprint (arXiv:1605.08032)
Friesen R. K., Pon A., Bourke T. L., Caselli P., Di Francesco J., Jørgensen J. K., Pineda J. E., 2018, ApJ, 869, 158
Fuente A. et al., 2017, A&A, 606, L3
Furuya K., Aikawa Y., Tomida K., Matsumoto T., Saigo K., Tomisaka K., Hersant F., Wakelam V., 2012, ApJ, 758, 86
Garrod R. T., Wakelam V., Herbst E., 2007, A&A, 467, 1103
Gerin M., Pety J., Fuente A., Cernicharo J., Commerçon B., Marcelino N., 2015, A&A, 577, L2
Grady C. A. et al., 2013, ApJ, 762, 48
Graedel T. E., Langer W. D., Frerking M. A., 1982, ApJS, 48, 321
Grassi T., Bovino S., Schleicher D. R. G., Prieto J., Seifried D., Simoncini E., Gianturco F. A., 2014, MNRAS, 439, 2386
Harries T. J., 2000, MNRAS, 315, 722
Harries T. J., 2011, MNRAS, 416, 1500
Hennebelle P., Fromang S., 2008, A&A, 477, 9

Hincelin U., Wakelam V., Hersant F., Guilloteau S., Loison J. C., Honvault P., Troe J., 2011, A&A, 530, A61
Hincelin U., Commerçon B., Wakelam V., Hersant F., Guilloteau S., Herbst E., 2016, ApJ, 822, 12
Hindmarsh A. C., 1983, IMACS Trans. Sci. Comput., 1, 55
Hirano N., Liu F.-c., 2014, ApJ, 789, 50
Jenkins E. B., 2009, ApJ, 700, 1299
Jørgensen J. K. et al., 2013, ApJ, 779, L22
Larson R. B., 1969, MNRAS, 145, 271
Lewis B. T., Bate M. R., 2017, MNRAS, 467, 3324
Lewis B. T., Bate M. R., Price D. J., 2015, MNRAS, 451, 288
Machida M. N., Inutsuka S.-i., Matsumoto T., 2008, ApJ, 676, 1088
Maret S., Bergin E. A., Tafalla M., 2013, A&A, 559, A53
Mathis J. S., Rumpl W., Nordsieck K. H., 1977, ApJ, 217, 425
Maury A. J., André P., Men'shchikov A., Könyves V., Bontemps S., 2011, A&A, 535, A77
McMullin J. P., Waters B., Schiebel D., Young W., Golap K., 2007, in Shaw R. A., Hill F., Bell D. J., eds, ASP Conf. Ser. 376, Astronomical Data Analysis Software and Systems XVI. Astron. Soc. Pac., San Francisco, CA, p. 127
Murillo N. M., van Dishoeck E. F., van der Wiel M. H. D., Jørgensen J. K., Drozdovskaya M. N., Calcutt H., Harsono D., 2018, A&A, 617, A120
Ohashi N. et al., 2014, ApJ, 796, 131
Pérez L. M. et al., 2016, Science, 353, 1519
Pezzuto S. et al., 2012, A&A, 547, A54
Pineda J. E. et al., 2011, ApJ, 743, 201
Pratap P., Dickens J. E., Snell R. L., Miralles M. P., Bergin E. A., Irvine W. M., Schloerb F. P., 1997, ApJ, 486, 862
Price-Whelan A. M. et al., 2018, AJ, 156, 123
Price D. J., 2007, PASA, 24, 159
Price D. J., Bate M. R., 2007, MNRAS, 377, 77
Price D. J., Monaghan J. J., 2005, MNRAS, 364, 384
Reboussin L., Wakelam V., Guilloteau S., Hersant F., 2014, MNRAS, 440, 3557
Rundle D., Harries T. J., Acreman D. M., Bate M. R., 2010, MNRAS, 407, 986
Saigo K., Tomisaka K., 2006, ApJ, 645, 381
Stolker T. et al., 2016, A&A, 595, A113
Tobin J. J. et al., 2015, ApJ, 798, 128
Tomida K., Okuzumi S., Machida M. N., 2015, ApJ, 801, 117
Tomisaka K., 2002, ApJ, 575, 306
Tomisaka K., Tomida K., 2011, PASJ, 63, 1151
Tricco T. S., Price D. J., 2012, J. Comput. Phys., 231, 7214
Tricco T. S., Price D. J., 2013, MNRAS, 436, 2810
Tsitali A. E., Belloche A., Commerçon B., Menten K. M., 2013, A&A, 557, A98
van Weeren R. J., Brinch C., Hogerheijde M. R., 2009, A&A, 497, 773
Wakelam V., Herbst E., 2008, ApJ, 680, 371
Wakelam V. et al., 2012, ApJS, 199, 21
Wakelam V. et al., 2015, ApJS, 217, 20
Whitehouse S. C., Bate M. R., 2006, MNRAS, 367, 32
Whitehouse S. C., Bate M. R., Monaghan J. J., 2005, MNRAS, 364, 1367
Wurster J., Bate M. R., Price D. J., 2018, MNRAS, 475, 1859
Young A. K., Bate M. R., Mowat C. F., Hatchell J., Harries T. J., 2018, MNRAS, 474, 800

APPENDIX: COMPARISON TO THE KIDA 2014 NETWORK

We performed the chemical calculations again for the MHD model with the gas-phase reactions from KIDA 2014 network (Wakelam et al. 2015) to examine how the results might differ. The gas-grain reactions which were added to the KIDA network separately remain unchanged. Figs A1 and A2 show the resulting abundance profiles averaged in the plane of the disc and the rotation axis, respectively.

The abundance profiles are mostly very similar with the 2011 and 2014 KIDA networks because it is the gas-grain reactions which drive the abundances outside of the FHSC. The snapshot taken during the first collapse (a) shows higher central abundances for CO and HCO^+. This is simply because the desorption of these species happens very quickly at this stage so the abundances increase rapidly and the exact abundance is sensitive to the exact moment it is measured. For CO, the peak abundance in the FHSC is slightly lower early in the FHSC stage but reaches $\sim 1 \times 10^{-4}$ by late in the FHSC stage, as it did with the KIDA 2011 network. The sublimation radius extends to 20 au in the plane of the disc, as before. The SO abundance is slightly higher deep within the FHSC but the profiles are very similar. The abundances profiles of HCO^+ are very similar for both networks. With the 2014 network, the CS abundance may be nearly an order of magnitude higher deep within the FHSC ($r \lesssim 3$ au). Comparing all of the molecular profiles shown in Figs 7 and 8 with those in Figs A1 and A2, only OCS has substantially different abundances over a wide range of radii.

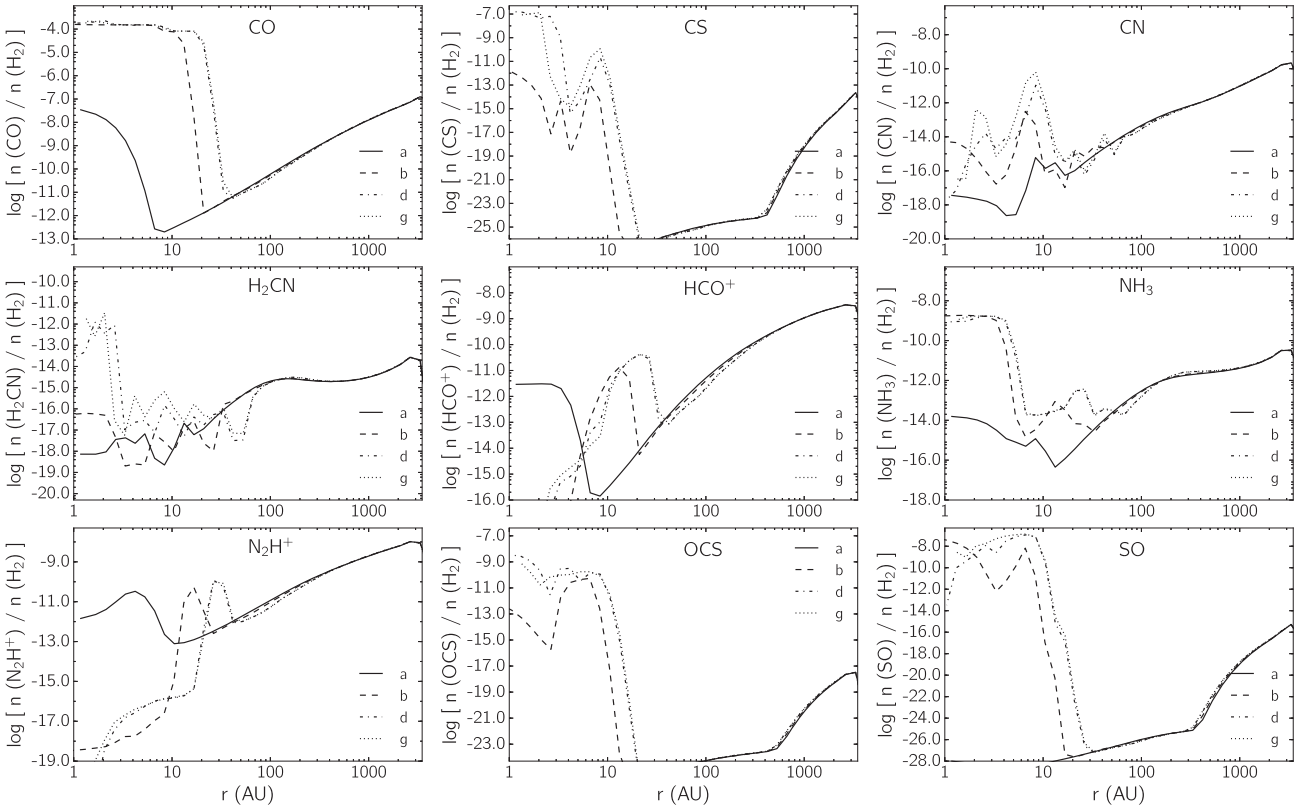

Figure A1. Average abundances of selected species from the MHD model perpendicular to the rotation axis, calculated using the KIDA 2014 chemical network.

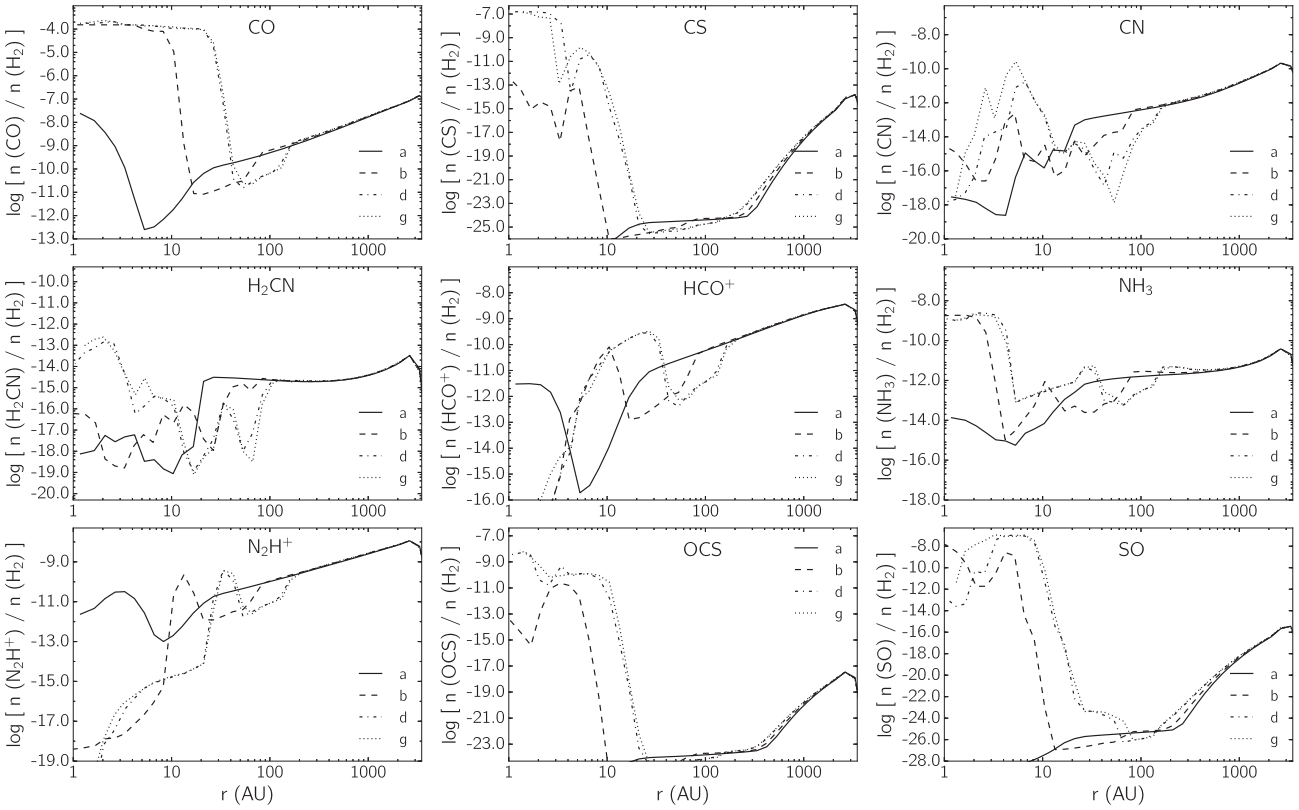

Figure A2. Average abundances of selected species from the MHD model parallel to the rotation axis, calculated using the KIDA 2014 chemical network.

This paper has been typeset from a TEX/LATEX file prepared by the author.